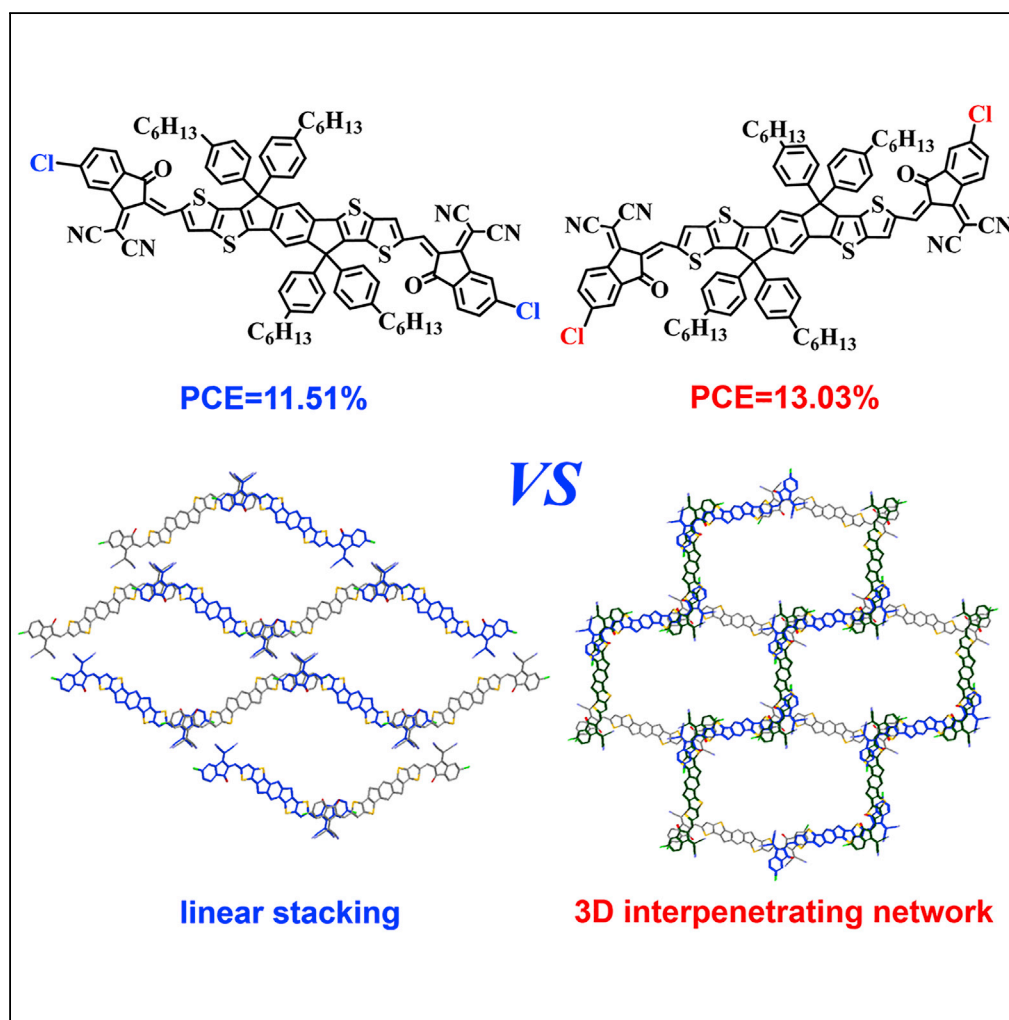


Article

Isomer-free: Precise Positioning of Chlorine-Induced Interpenetrating Charge Transfer for Elevated Solar Conversion



Hanjian Lai, Hui Chen, Jiadong Zhou, ..., Nan Zheng, Zengqi Xie, Feng He

hef@sustech.edu.cn

HIGHLIGHTS

Isomer-free: improved phase purity for high-performance non-fullerene acceptor

Chlorine-substitution fine-tuned the configurations and properties of molecules

Precise Cl-atom substitution induced 3D interpenetrating network charge transfer

ITIC-2Cl- γ exhibited higher PCE of 13.03% and better stability

Lai et al., iScience 17, 302–314
July 26, 2019 © 2019 The Authors.
<https://doi.org/10.1016/j.isci.2019.06.033>

Article

Isomer-free: Precise Positioning of Chlorine-Induced Interpenetrating Charge Transfer for Elevated Solar Conversion

Hanjian Lai,^{1,2,4} Hui Chen,^{1,4} Jiadong Zhou,^{3,4} Jianfei Qu,¹ Pengjie Chao,¹ Tao Liu,¹ Xiaoyong Chang,¹ Nan Zheng,³ Zengqi Xie,³ and Feng He^{1,5,*}

SUMMARY

The influence caused by the position of the chlorine atom on end groups of two non-fullerene acceptors (ITIC-2Cl- δ and ITIC-2Cl- γ) was intensely investigated. The single-crystal structures show that ITIC-2Cl- γ has a better molecular planarity and closer π - π interaction distance. More importantly, a 3D rectangle-like interpenetrating network is formed in ITIC-2Cl- γ and is beneficial to rapid charge transfer along multiple directions, whereas only a linear stacked structure could be observed in ITIC-2Cl- δ . The two acceptor-based solar cells show power conversion efficiencies (PCEs) over 11%, higher than that of the ITIC-2Cl-*m*-based device (10.85%). An excellent PCE of 13.03% is obtained by the ITIC-2Cl- γ -based device. In addition, the ITIC-2Cl- γ -based device also shows the best device stability. This study indicates that chlorine positioning has a great impact on the acceptors; more importantly, the 3D network structure may be a promising strategy for non-fullerene acceptors to improve the PCE and stability of organic solar cells.

INTRODUCTION

In the past two decades, fullerene and its derivative-based acceptors have dominated the field of organic solar cells (OSCs) with a power conversion efficiency over 11% (Zhao et al., 2016; He et al., 2015; Li et al., 2014; Ouyang et al., 2015; Liu et al., 2014). The isotropic feature of fullerene-type acceptors, especially the widely used [6,6]-phenyl-C61-butyric acid methyl ester (PC₆₁BM) and [6,6]-phenyl-C71-butyric acid methyl ester (PC₇₁BM), endows materials with three-dimensional (3D) isotropic charge transport, and such compounds have been a good choice as acceptors in OSC applications over the past 20 years. Furthermore, the fullerene acceptors also show broad applicability when blended with various donor materials. However, there are also clear drawbacks to fullerene-based acceptors (FAs), such as weak absorption in the visible and near-infrared regions, poor photothermal stability, and difficulty in purification. In addition, the power conversion efficiencies (PCEs) failed to surpass 12% for several years (Nielsen et al., 2015; Holliday et al., 2016; Cha et al., 2017). Therefore, there has been an urgent need to develop next-generation acceptors, such as non-fullerene acceptors (NFAs) with a strong absorption, to overcome the deficiencies of FAs (Wadsworth et al., 2018; Cheng et al., 2018). Excitingly, a star acceptor named 3,9-bis(2-methylene-(3-(1,1-dicyanomethylene)-indanone))-5,5,11,11-tetrakis(4-hexylphenyl)-dithieno [2,3-d':2',3'-d']-s-indaceno [1,2-b:5,6-b']-dithiophene (ITIC) was reported by Zhan and coworkers in 2015 and opened a new avenue to increase the OSC performance (Lin et al., 2015). Subsequently, a series of acceptor-donor-acceptor (A-D-A)-type molecules were designed and synthesized with indacenodithiophene (IDT) or indacenodithieno[3,2-b]thiophene (IDTT) as the electron-donating core and 1,1-dicyanomethylene-3-indanone (IC) or its derivatives as electron-accepting end groups (Lin et al., 2015, 2016; Kan et al., 2017a, 2017b; Yang et al., 2016). The PCE of the NFA-based OSCs exceeded 13% in rapid time (Hou et al., 2018; Li et al., 2018a, 2018b, 2018c, 2018d; Wang et al., 2019; Fan et al., 2018a, 2018b; Zhang et al., 2018a, 2018b, 2018c, 2018d; Li et al., 2018a, 2018b, 2018c, 2018d; Fan et al., 2018a, 2018b; Sun et al., 2018; Che et al., 2018; Zhang et al., 2018a, 2018b, 2018c, 2018d; Cui et al., 2017a, 2017b; Xu et al., 2018).

The rapid development of NFAs benefits from tunable optoelectronic properties by core modifications (Xiao et al., 2017; Swick et al., 2018; Gao et al., 2018a, 2018b; Yao et al., 2018), side chain engineering (Fei et al., 2018; Wang et al., 2017; Kan et al., 2017a, 2017b; Feng et al., 2017), and functional group modulations (Aldrich et al., 2019; Wang et al., 2018a, 2018b; Yang et al., 2017). For instance, a very simple

¹Department of Chemistry and Shenzhen Grubbs Institute, Southern University of Science and Technology, Shenzhen 518055, China

²School of Chemistry and Chemical Engineering, Harbin Institute of Technology, Harbin 150001, China

³Institute of Polymer Optoelectronic Materials and Devices, State Key Laboratory of Luminescent Materials and Devices, South China University of Technology, Guangzhou 510640, China

⁴These authors contributed equally

⁵Lead Contact

*Correspondence: hef@sustech.edu.cn

<https://doi.org/10.1016/j.isci.2019.06.033>

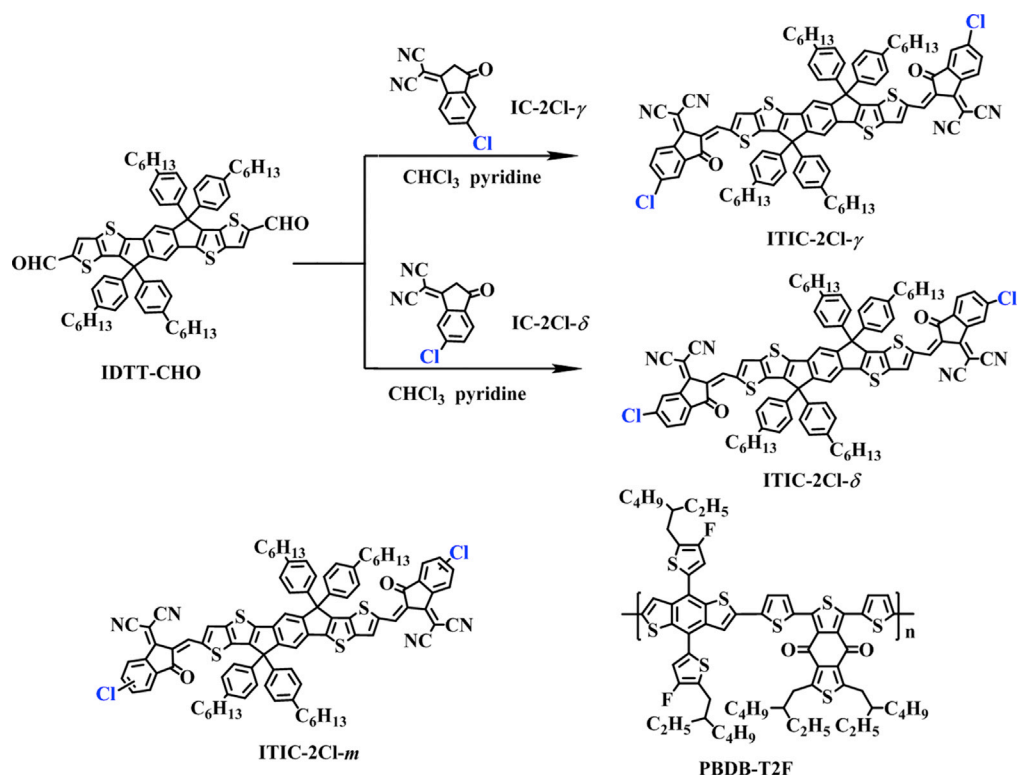


but effective method, halogenation, was used to modify the electron-withdrawing ability (Wang et al., 2018a, 2018b; Yang et al., 2017). Within this method, chlorination is an effective approach for chemical modification benefiting from special properties, such as a more efficient downshift of energy levels, the ability to broaden and enhance absorption, and a facile synthesis, which would be conducive to the commercialization of OSCs (Zhang et al., 2018a, 2018b, 2018c, 2018d; Cui et al., 2017a, 2017b; Li et al., 2017; Zhang et al., 2017; Chao et al., 2018; Mo et al., 2017; Kan et al., 2017a, 2017b). Several works have reported that a mixture of two kinds of monochlorinated IC end group isomers (IC-Cl-*m*) was used as NFAs with an enhanced solar energy conversion (Zhang et al., 2018a, 2018b, 2018c, 2018d; Wang et al., 2018a, 2018b; Chen et al., 2018; Xie et al., 2018). However, the non-site specificity of the single chlorine atom in these efforts would result in a disordered morphology with lower efficiencies owing to the isomer impurity of the final acceptor, and the batch-to-batch variation will also bring a large deviation in the performance of the corresponding OSC devices. Furthermore, in theory, the optoelectronic performance of each isomer should be different due to different electronic, optical, charge transport, and morphological properties (Wang et al., 2018a, 2018b), resulting in the performances we observe in this study.

In this study, two end groups IC-Cl- δ and IC-Cl- γ were obtained from IC-Cl-*m* by various purifications. In detail, the mixture can be recrystallized from chloroform and ethanol to yield high-quality IC-Cl- δ and IC-Cl- γ , respectively. Therefore, two NFAs ITIC-2Cl- δ and ITIC-2Cl- γ could be synthesized by the Knoevenagel condensation reaction with a chlorine atom at a specific position on the IC end groups. In this way, the isomer problem was resolved on the synthetic side. Interestingly, ITIC-2Cl- δ and ITIC-2Cl- γ exhibit completely different single-crystal structures from single-crystal X-ray diffraction (XRD) analysis due to the different positions of the chlorine atom on the end groups. ITIC-2Cl- δ shows a linear stacked structure in the single crystal, which is similar to what has been discovered in some reported NFA systems (Yan et al., 2018; Qu et al., 2018). The charge carriers should be dominantly transported in one direction, with contributions from the stronger electron hopping along the horizontal intermolecular packing, and then transported by the well-ordered end group tunnels. Although a 3D interpenetrating network structure is observed in the ITIC-2Cl- γ single crystal, in detail, there is one more group of molecules in the perpendicular direction, aligned almost 90° to the horizontal group of molecules to form a rectangle-like interpenetrating charge carrier transport system. This arrangement would definitely facilitate charge transport in horizontal and perpendicular directions, similar to the isotropic transmission properties of fullerene acceptors, and an excellent PCE of over 13% is therefore obtained by ITIC-2Cl- γ -based device. This value is approximately 13.2% higher than that of ITIC-2Cl- δ -based device without interpenetrating charge carrier transport, and 20.1% higher than that of the mixed ITIC-2Cl-*m*-based device. This demonstrates that the purity of the NFA, even one with only different isomers, is very important to promote the OSC efficiency. The more important information we deliver here is that the 3D interpenetrating charge carrier transport or more ideal isotropic transmission properties in fullerene acceptors may be a promising design strategy for high-performance NFAs.

RESULTS AND DISCUSSION

IC-Cl-*m* was synthesized from 4-chlorophthalic anhydride in two steps, as reported previously (Zhao et al., 2017; Shi et al., 2017; Xie et al., 2017). As shown in Scheme 1, the synthetic routes of ITIC-2Cl- δ and ITIC-2Cl- γ are quite straightforward, in which the key point lies in the successful separation of the mixed monomers of IC-Cl- δ and IC-Cl- γ from recrystallization with selected solvents. In detail, the two isomers from the previous cyclization reaction can be purified by recrystallization from ethanol to yield about 500 mg IC-Cl- γ and then from chloroform to obtain about 1 g IC-Cl- δ by 3 g of IC-Cl-*m*. The IC-Cl-*m* could be recycled for the next recrystallization (Figure 1A). Figure 1C shows the ¹H-NMR of the aromatic region of the purified isomers IC-Cl- δ and IC-Cl- γ and mixture of monomers IC-Cl-*m*. IC-Cl-*m* is composed of 64% IC-Cl- δ and 36% IC-Cl- γ from the ¹H-NMR analysis. In addition, the peak shapes of IC-Cl- δ and IC-Cl- γ are completely different in the ¹H-NMR. IC-Cl- γ shows a doublet at the ϵ position, whereas IC-Cl- δ shows a single peak at this position (approximately 8.61 ppm). To further prove the location of the chlorine atom on the end group, the single crystals of IC-Cl- δ and IC-Cl- γ were prepared and are shown in Figure 1B. The final small molecules, ITIC-2Cl- δ and ITIC-2Cl- γ , were synthesized by Knoevenagel condensation reactions between IDTT-CHO and IC-Cl- δ and IC-Cl- γ , respectively. ITIC-2Cl-*m* was also synthesized according to the literature for comparison (Xiao et al., 2017). The synthesis and purification details are provided in the Supplemental Information. The three small molecules show good solubility in common solvents, such as dichloromethane, chloroform, or chlorobenzene. PBDB-T2F was used as polymer donor as shown in Scheme 1, which shows a number-average molecular weight (M_n) of 48.0 kDa, and a polydispersity index of 2.41 measured by high-temperature gel permeation chromatography at 150°C with 1,2,4-trichlorobenzene solvent.



Scheme 1. The Synthetic Routes of ITIC-2Cl- δ and ITIC-2Cl- γ , and the Structures of ITIC-2Cl-*m* and PBDB-T2F

Also see Figures S4–S8.

The charge transport properties in bulk-heterojunction (BHJ) blends can be understood, and the rational design of new materials can be instructed from complementary insight into structure or self-assembly relationships by the analysis of molecular single-crystal packing (Swick *et al.*, 2018; Gao *et al.*, 2018a, 2018b). Single-crystal XRD analysis was used to identify the influence of the position of chlorine substitution on the end IC groups to the molecular configuration and packing in the condensed state. Single crystals of ITIC-2Cl- δ and ITIC-2Cl- γ were obtained by the conventional slow diffusion method (chloroform is a good solvent and ethanol is a poor solvent). As shown in Figure S1 (in the Supplemental Information), both ITIC-2Cl- δ and ITIC-2Cl- γ have good planarity in one molecule but do show a twist angle difference between the end group and the core. The dihedral angle between the IDTT core and the end group in ITIC-2Cl- γ is only 1.32° , whereas ITIC-2Cl- δ shows a larger dihedral angle of 4.51° , indicating that the position of the chlorine atom in the end group has a great effect on the molecular configuration.

Figure 2 shows the relatively close π - π interactions in both small molecules owing to the multiple interlocked $\text{Cl}\cdots\text{S}$, $\text{Cl}\cdots\pi$, and $\text{S}\cdots\text{O}$ interactions between adjacent molecules (shown in Figure S2), which lead to the formation of *J*-aggregation in the horizontal direction, as shown in Figure 2. In detail, Figure 2A shows two kinds of orientations in the ITIC-2Cl- δ single crystal (colored gray and blue) with a dihedral angle of 9.3° , and the π - π distances are approximately 3.48 Å and 3.46 Å. However, there are three kinds of orientations in the single-crystal of ITIC-2Cl- γ (colored gray, green, and blue), as shown in Figure 2B; the dihedral angle of two adjacent molecules in the horizontal direction is decreased to approximately 4.0° , and there is one more group of molecules with a perpendicular direction to form a rectangular interlocked molecular structure with a length of 35.6 Å and a width of 21.3 Å. This way, the π - π interaction distances are dramatically decreased (Figure 2B, 3.35 Å, 3.38 Å, and 3.40 Å) compared with those in ITIC-2Cl- δ molecules. The decreased π - π distances of ITIC-2Cl- γ should be induced by multiple $\text{Cl}\cdots\pi$, $\text{S}\cdots\text{O}$, and closer $\text{Cl}\cdots\text{S}$ interactions (Figure S2) between three adjacent ITIC-2Cl- γ molecules and better planarity in one ITIC-2Cl- γ molecule, which should be beneficial for the charge transport between horizontally connected molecules.

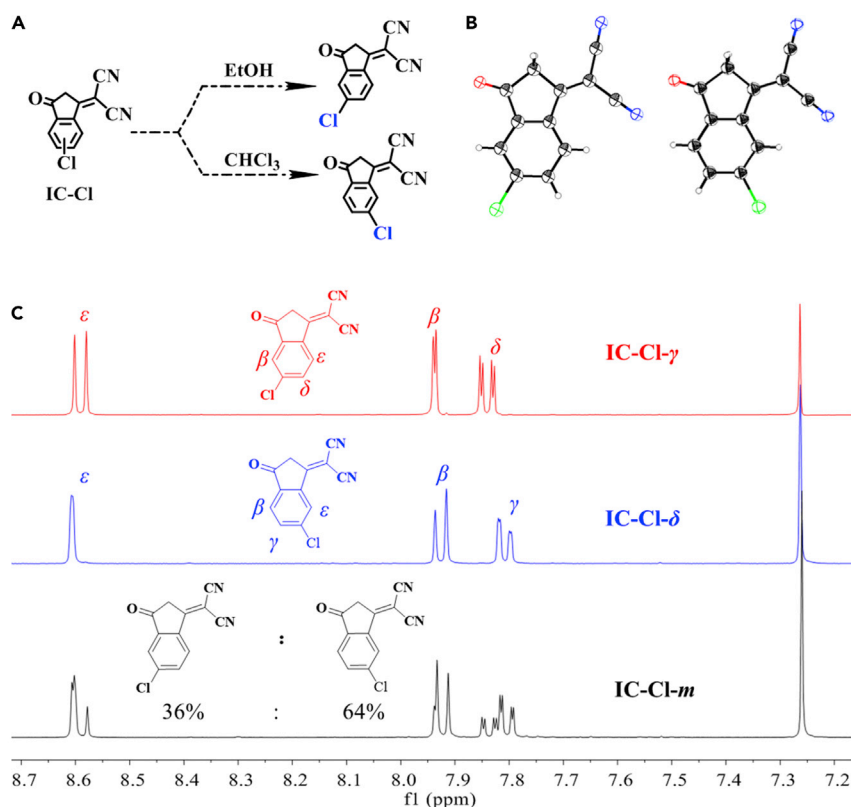


Figure 1. Purification Method, Single-crystal Structures and ¹H-NMR Spectra of Monomers

(A) Methods to purify IC-Cl-δ and IC-Cl-γ.

(B) Single-crystal structures of IC-Cl-δ, and IC-Cl-γ.

(C) The ¹H-NMR of the aromatic region of IC-Cl-γ, IC-Cl-δ, and IC-Cl-m.

Also see [Scheme S1](#).

As discussed above, it is worth noting that only a linear stacked structure could be observed in ITIC-2Cl-δ (Figures 3A and 3B) and the majority of electrons may be transmitted along the horizontal π - π stacking direction, whereas ITIC-2Cl-γ shows one more group of molecules in the perpendicular direction, which is oriented almost 90° to the horizontal group of molecules. As shown in Figures 3C and 3D, the single-crystal structure of ITIC-2Cl-γ finally presents a 3D interpenetrating network to form a kind of rectangular structure. The 3D interpenetrating network structure will clearly facilitate charge transport in all directions, similar to the isotropic transmission properties of fullerene-type acceptors. These results indicate that the different substitution positions of the chlorine atom on the IC end group play a very important role in molecular configuration and packing, which would contribute to form significantly different crystal types. The 3D rectangle-like interpenetrating network structure endows multiple electron transport tunnels to ITIC-2Cl-γ that are very similar to that of the isotropic electron transmission in classical fullerene acceptors. This motif would definitely promote electron transport in the acceptor, which will also afford a higher electron mobility in blend films for better organic photovoltaic (OPV) device performance.

The thermal properties of the three small molecules were characterized by thermogravimetric analysis and differential scanning calorimetry (DSC). As shown in Figure S9 (in the [Supplemental Information](#)), ITIC-2Cl-δ, ITIC-2Cl-m, and ITIC-2Cl-γ exhibit good thermal stabilities with 5% weight loss temperatures (T_d) of 320°C, 316°C, and 341°C, respectively. This result indicates that ITIC-2Cl-γ is more thermally stable than ITIC-2Cl-δ, whereas ITIC-2Cl-m shows the worst thermal stability of the three molecules. The highest thermal stability of ITIC-2Cl-γ among these molecules could be attributed to the 3D rectangle-like interpenetrating network with enhanced intermolecular interactions by the introduction of chlorine at the γ position, as discussed above. DSC shows there are no apparent crystallization or melting peaks up to 250°C for the three small molecules in their DSC traces, which indicates that these three molecules are

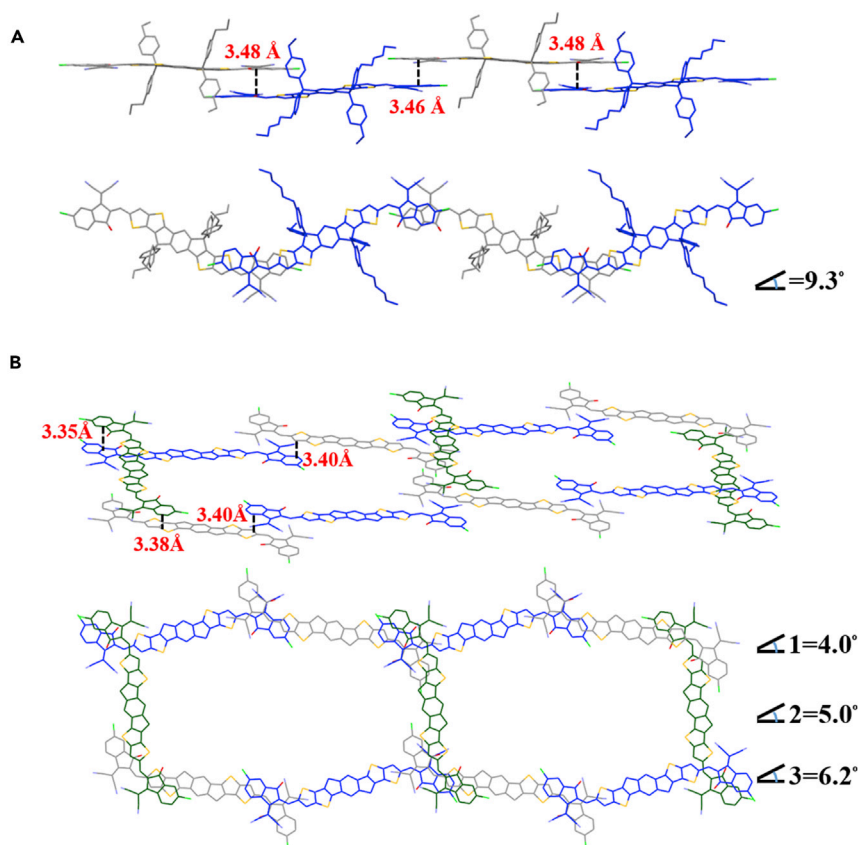


Figure 2. X-Ray Crystallographic Structures and Dihedral Angles of Two Adjacent Cores of ITIC-2Cl- δ and ITIC-2Cl- γ

(A) X-ray crystallographic structures of ITIC-2Cl- δ and the dihedral angles (9.3°) of two adjacent cores.

(B) X-ray crystallographic structures of ITIC-2Cl- γ and the dihedral angles of each two adjacent cores: angle 1 is 4.0° (colored blue and gray), angle 2 is 5.0° (colored green and blue), and angle 3 is 6.2° (colored green and gray). (The hexyl benzene side chains of ITIC-2Cl- γ in Figure 2B were neglected for clarity).

Also see Figures S1 and S2.

all suitable for subsequent device fabrication with sufficient thermal stability because of the strong intermolecular interactions.

Figures 4A and 4B show the ultraviolet-visible (UV-vis) absorption spectra of ITIC-2Cl- δ , ITIC-2Cl- m , and ITIC-2Cl- γ in chloroform solution (10^{-5} mol L $^{-1}$) and in thin films, respectively. All three molecules show a strong absorption in the wavelength range of 600–750 nm with maximum absorption peaks at 693, 692, and 690 nm for ITIC-2Cl- δ , ITIC-2Cl- m , and ITIC-2Cl- γ , respectively. The extinction coefficients of the molecules are 1.64×10^5 , 1.86×10^5 , and 2.00×10^5 L mol $^{-1}$ cm $^{-1}$, respectively, which indicates that the different substitution positions of the chlorine atom on the IC end group can directly affect the absorption properties of the molecules by enhanced intermolecular interactions. The maximum absorption peaks of ITIC-2Cl- δ , ITIC-2Cl- m , and ITIC-2Cl- γ films are 734, 727, and 721 nm, respectively. Compared with the absorption in solution, significant redshifts of 41, 35, and 31 nm are observed in the film states, which show strong aggregation in the films. It is worth noting that the maximum absorption peak of ITIC-2Cl- γ is blue-shifted by 13 nm in the solid state compared with that of ITIC-2Cl- δ , and this can be explained by the slightly reduced *J*-aggregation feature in the single-crystal structure of ITIC-2Cl- γ . The IDTT cores of ITIC-2Cl- γ overlap slightly more than those of ITIC-2Cl- δ . The angle between two adjacent ITT core centers and the molecular plane of ITIC-2Cl- γ is 13.00° , which is larger than that of ITIC-2Cl- δ (11.48°). This result implies that ITIC-2Cl- δ is more inclined to ideal *J*-aggregation, which slightly redshifts the absorption of ITIC-2Cl- δ in the solid state (Cai et al., 2018; Hestand and Spano, 2017). However, the IC end group of ITIC-2Cl- γ shows slightly more overlap with less *J*-aggregation, which will enhance the intermolecular

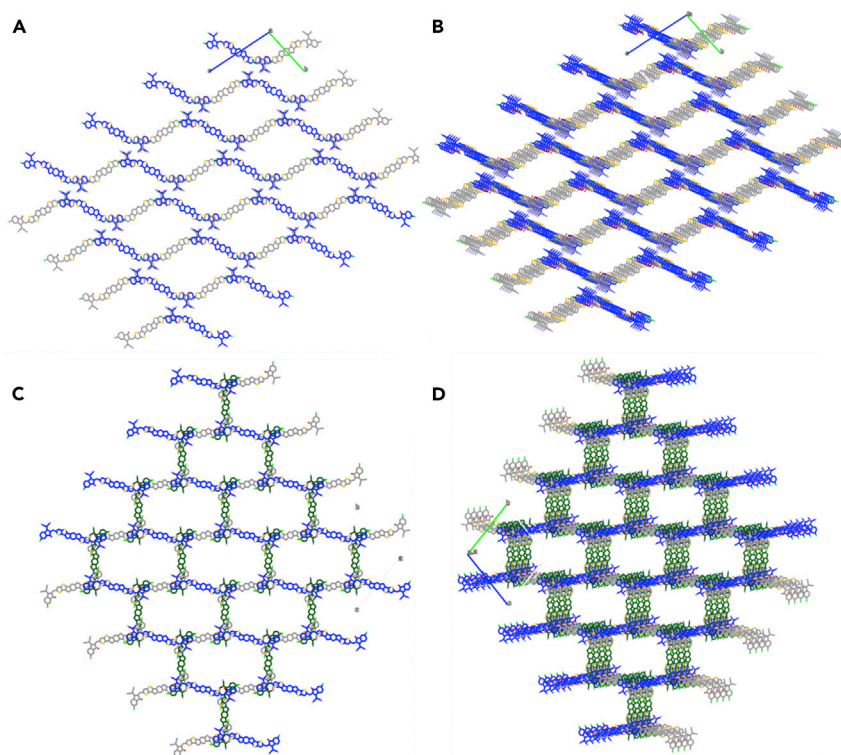


Figure 3. Crystal Packing Diagrams for ITIC-2Cl- δ and ITIC-2Cl- γ

(A and B) (A) Top view of ITIC-2Cl- δ . (B) Side view of ITIC-2Cl- δ .

(C and D) (C) Top view of ITIC-2Cl- γ . (D) Side view of ITIC-2Cl- γ . (The hexyl benzene side chains were neglected for clarity and better comparison; the full crystal packing diagrams with hexyl benzene side chains are shown in Figure S3).

Also see Figure S3.

charge transfer between such molecules and favor the carrier transport in final OPV devices. The UV-vis absorption spectra of the blend films of PBDB-T2F: ITIC-2Cl- δ , PBDB-T2F: ITIC-2Cl- m , and PBDB-T2F: ITIC-2Cl- γ are shown in Figure 4C. The intensity of the peak in the long-wavelength region of ITIC-2Cl- γ (721 nm) is the highest and corresponds to the strongest π - π intermolecular interaction among the three blend films. Interestingly, the intensity of ITIC-2Cl- δ is slightly higher than that of ITIC-2Cl- m in the blend films, which is contrary to the extinction coefficients of the two molecules, indicating a π - π interaction in the PBDB-T2F: ITIC-2Cl- δ film stronger than that in the ITIC-2Cl- m blend film. The mixed ITIC-2Cl- m would affect the molecular packing because of the multiple molecular arrangements, thus leading to a low extinction coefficient in its blend film. These results indicate that the different positions of the chlorine atom on the end group have a great influence on the absorption properties. Furthermore, it is of great importance to avoid using the mixture for better molecular packing and enhanced absorption. In addition, it is suggested that the 3D rectangle-like interpenetrating network structure of ITIC-2Cl- γ is more favored to maintain the π - π intermolecular interactions in the blend film state. The strategy of a 3D interpenetrating network design in NFAs may be a promising way to elevate the carrier transport and enhance the final solar conversion.

The electrochemical properties of ITIC-2Cl- δ , ITIC-2Cl- m , and ITIC-2Cl- γ were measured by cyclic voltammetry and are shown in Figures 4D and S10 (in the Supplemental Information). The highest occupied molecular orbital (HOMO) energy levels of ITIC-2Cl- δ , ITIC-2Cl- m , and ITIC-2Cl- γ are estimated to be -5.53 , -5.54 and -5.55 eV, respectively, and the lowest unoccupied molecular orbital (LUMO) energy levels are -3.94 , -3.93 , and -3.92 eV, respectively (as referenced to the ferrocene/ferrocenium [Fc/Fc⁺] redox couple). The LUMO and HOMO energies of PBDB-T2F are -5.45 eV and -3.65 eV (Zhang et al., 2018c), respectively. Compared with the levels in ITIC-2Cl- δ , ITIC-2Cl- γ exhibits a 0.02 eV higher LUMO energy and 0.02 eV lower HOMO energy, as a result of a wider band gap of 1.63 eV than the 1.59 eV for ITIC-2Cl- δ . This result is in accordance with the blueshift of the absorption spectrum and the greater

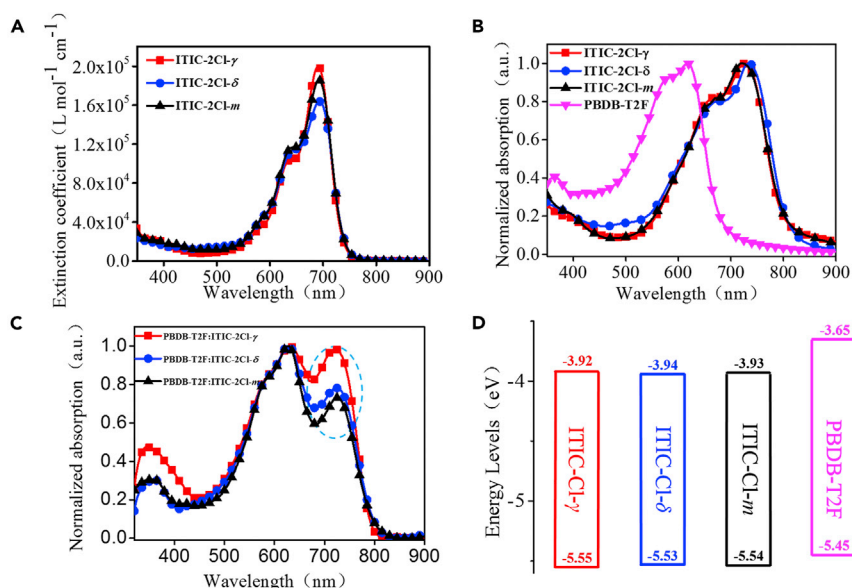


Figure 4. Optical and Electrical Properties of ITIC-2Cl- δ , ITIC-2Cl- m , and ITIC-2Cl- γ

(A) Absorption spectra of the three small molecules in chloroform solution at a concentration of 10^{-5} mol L $^{-1}$.

(B) Normalized UV-vis absorption spectra of the three small molecules and PBDB-T2F in films.

(C) Normalized UV-vis absorption spectra of PBDB-T2F:ITIC-2Cl- δ , PBDB-T2F:ITIC-2Cl- m , and PBDB-T2F:ITIC-2Cl- γ blend films.

(D) Energy level diagrams of ITIC-2Cl- δ , ITIC-2Cl- m , ITIC-2Cl- γ , and the donor PBDB-T2F.

Also see [Figures S9](#) and [S10](#).

overlap of the IC end groups (less J -aggregation) in ITIC-2Cl- γ (Figure 4B). In addition, the higher LUMO energy of ITIC-2Cl- γ would benefit a higher open-circuit voltage in solar devices.

To evidence the application of these small molecules as prospective acceptors in photovoltaics, devices with an inverted structure of ITO/ZnO/active layer/MoO $_3$ /Ag were used to investigate the performance of OSCs from the three small molecules in blends with polymer PBDB-T2F (structure is shown in Scheme 1). The current density-voltage (J - V) curves are shown in Figure 5A, and the extracted photovoltaic parameters of the three PSC devices are listed in Table 1. The optimal donor: acceptor weight ratio is 1:1, with a total concentration of 20 mg mL $^{-1}$ in a chlorobenzene solution including 0.5% 1,8-diiodooctane as an additive. The PBDB-T2F:ITIC-2Cl- m -based device shows an inferior PCE of 10.85% with a fill factor (FF) of 66.86%, which could be caused by the poor molecular packing of the mixed ITIC-2Cl- m . The PBDB-T2F:ITIC-2Cl- δ -based device has a larger PCE of 11.51% with an open-circuit voltage (V_{OC}) of 0.90 V, a short-circuit current density (J_{SC}) of 18.34 mA cm $^{-2}$, and an FF of 69.87%. However, the PBDB-T2F:ITIC-2Cl- γ -based device presents a higher V_{OC} of 0.93 V, J_{SC} of 18.94 mA cm $^{-2}$, and improved FF of approximately 74.07%, leading to the highest PCE of 13.03%. The outstanding performance should benefit from the higher LUMO energy level, higher absorption coefficient, and 3D interpenetrating network structure of ITIC-2Cl- γ . These results indicate that the purity of the active materials and the position of the chlorine atom on the end group could lead to huge differences in device performance, such as over a 20.1% enhancement in PCE when going from the mixed ITIC-2Cl- m to the γ -substituted ITIC-2Cl- γ . To further analyze the J_{SC} effects in these devices, the external quantum efficiency (EQE) spectra of the PBDB-T2F: acceptor-based devices were acquired, and the curves are shown in Figure 5B. OSCs based on all three small molecules display a high photon response value of >60% from 460 to 760 nm. The main difference between the three curves is located at 540–740 nm and is in accordance with the absorption spectra of their blend films (Figure 4C). ITIC-2Cl- γ has the highest absorption coefficient, and the expected highest photon response is observed in the range of 460–760 nm, resulting in the highest J_{SC} in the corresponding device. The calculated J_{cal} of ITIC-2Cl- δ , ITIC-2Cl- m , and ITIC-2Cl- γ devices based on the EQE curves are 17.52 mA cm $^{-2}$, 17.26 mA cm $^{-2}$, and 18.16 mA cm $^{-2}$, respectively, and match well with the J_{SC} values from the above J - V test curves.

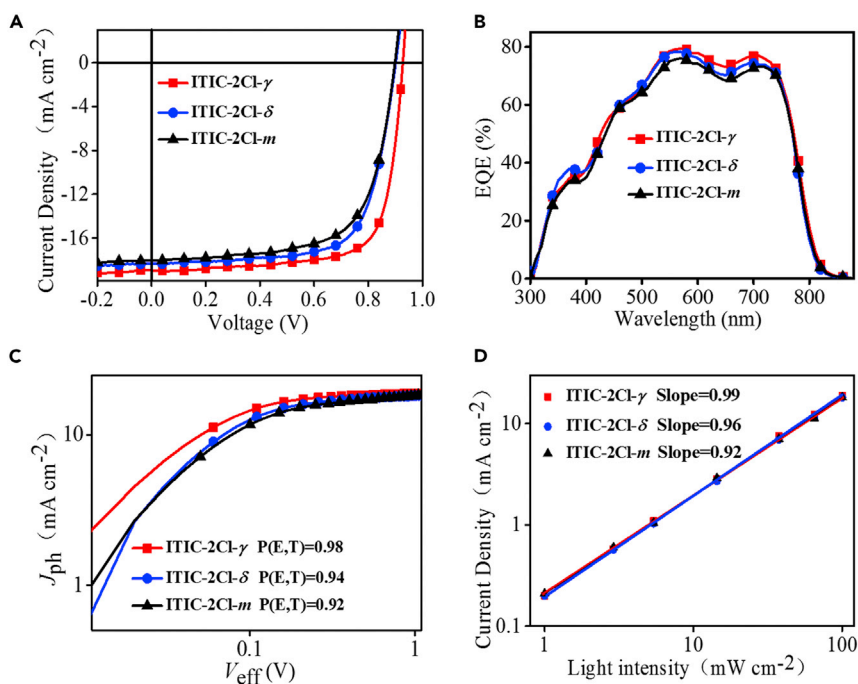


Figure 5. Device Performances Based on ITIC-2Cl- δ , ITIC-2Cl- m , and ITIC-2Cl- γ

(A) J–V curves of devices using different NFAs.

(B) EQE curves of the corresponding photovoltaic devices.

(C) Photocurrent density (J_{ph}) versus effective voltage (V_{eff}) characteristics.

(D) J_{SC} as a function of light intensity on a double-logarithmic scale for devices using different NFAs.

Also see [Figures S11](#) and [S14–S16](#) and [Tables S2](#) and [S3](#).

To understand the influence of the different positions of the chlorine atom on the end group on the exciton dissociation and carrier collection processes, the charge dissociation probabilities ($P(E,T) = J_{ph}/J_{sat}$) of the three small-molecule-based devices were determined, as shown in [Figure 5C](#). The **PBDB-T2F: ITIC-2Cl- γ** -based device shows the highest value (98%) for the calculated charge dissociation probability ($P(E,T)$) under J_{SC} conditions compared with that of the **PBDB-T2F: ITIC-2Cl- δ** -based device (94%) and **PBDB-T2F: ITIC-2Cl- m** -based device (92%). This result demonstrates the more efficient exciton dissociation at the interface between ITIC-2Cl- γ and **PBDB-T2F**, corresponding to the higher J_{SC} and FF of ITIC-2Cl- γ -based OSCs. [Figure 5D](#) shows the J_{SC} as a function of illumination intensity to further learn more about the process of carrier recombination, and the fitted slopes for ITIC-2Cl- δ , ITIC-2Cl- m , and ITIC-2Cl- γ -based devices are 0.96, 0.92 and 0.99, respectively. The highest value of 0.99 implies that the **PBDB-T2F: ITIC-2Cl- γ** -based device shows weak bimolecular recombination during operation. These results reveal that the different positions of the chlorine atom on the end group can influence exciton dissociation and bimolecular recombination; in particular, the lowest $P(E,T)$ value (92%) and the lowest slope (0.92) of the ITIC-2Cl- m -based device implies that avoiding acceptor mixtures is very important to obtain efficient exciton dissociation and reduced bimolecular recombination.

[Figure S11](#) shows the blended thin-film morphologies that were investigated by transmission electron microscopy (TEM) and atomic force microscopy (AFM). All three acceptor-based devices show similar film morphologies from the AFM results and exhibit smooth and uniform surfaces with relatively small root-mean-square roughness values of 2.11, 1.92, and 1.97 nm. The TEM image shows that the three acceptor-based devices have suitable phase separation sizes, which may help impart good transport properties to improve device performance.

To characterize the charge transport properties of the three small-molecule-based devices, the space charge limited current (SCLC) method was used to calculate the electron and hole mobilities, and the

Acceptors	V_{OC} (V)	J_{SC} ($\text{mA} \cdot \text{cm}^{-2}$)	FF (%)	PCE_{max} (%)	μ_h ($\text{cm}^2 \cdot \text{V}^{-1} \cdot \text{s}^{-1}$)	μ_e ($\text{cm}^2 \cdot \text{V}^{-1} \cdot \text{s}^{-1}$)	μ_h/μ_e
ITIC-2Cl- γ	0.93	18.94 (18.79 \pm 0.18)	74.07 (73.63 \pm 0.47)	13.03 (12.90 \pm 0.16)	4.5×10^{-4}	2.6×10^{-4}	1.7
ITIC-2Cl- δ	0.90	18.34 (18.06 \pm 0.28)	69.87 (69.32 \pm 0.52)	11.51 (11.25 \pm 0.31)	3.6×10^{-4}	1.2×10^{-4}	3.0
ITIC-2Cl- m	0.90	18.03 (17.85 \pm 0.21)	66.86 (66.25 \pm 0.56)	10.85 (10.61 \pm 0.28)	2.2×10^{-4}	9.5×10^{-5}	2.3

Table 1. Photovoltaic Parameters of the Optimized OSCs of ITIC-2Cl- δ , ITIC-2Cl- m , and ITIC-2Cl- γ -Based Devices

corresponding curves are shown in Figure 6A and Figure 6B with the calculated mobilities listed in Table 1. The electron-only devices display electron mobilities of 1.2×10^{-4} , 9.5×10^{-5} , and $2.6 \times 10^{-4} \text{ cm}^2 \text{ V}^{-1} \text{ s}^{-1}$ for ITIC-2Cl- δ , ITIC-2Cl- m , and ITIC-2Cl- γ , respectively, whereas the hole-only devices show hole mobilities 3.6×10^{-4} , 2.2×10^{-4} , and $4.5 \times 10^{-4} \text{ cm}^2 \text{ V}^{-1} \text{ s}^{-1}$, respectively, corresponding to hole-electron mobility ratios of 3.0, 2.3, and 1.7, respectively. ITIC-2Cl- m shows the lowest electron and hole mobilities, indicating that the worse molecular packing is unable to transport carriers efficiently. However, the highest and more balanced electron and hole mobilities are observed for ITIC-2Cl- γ , as a result of the 3D interpenetrating network structure that is beneficial to rapid charge transfer.

To further understand the dynamic behavior in devices, the transient photovoltage and transient photocurrent of three acceptor-based OSC devices were measured; the curves are shown in Figures 6C and 6D, and the extracted values of the carrier lifetime (τ) and the determined sweeping out times (t_s) are shown in Table S1. The τ of ITIC-2Cl- δ -, ITIC-2Cl- m -, and ITIC-2Cl- γ -based OSCs devices were 0.83, 0.74, and 1.12 μs , and the t_s of three devices were 0.31, 0.35, and 0.29 μs , respectively. The longest carrier lifetime and the lowest t_s value of ITIC-2Cl- γ -based OSCs corresponded to the most effective charge transport and collection in the device, whereas ITIC-2Cl- m -based device shows the lowest τ/t_s value of 2.11. It indicated that the presence of the mixture may increase the probability of bimolecular recombination and reduce carrier lifetime to further decrease the J_{SC} and FF of the devices, whereas the highest τ/t_s value of 3.86 was observed in ITIC-2Cl- γ -based OSC devices, which may benefit from the 3D rectangle-like interpenetrating network structure of ITIC-2Cl- γ and in agreement with the highest J_{SC} and FF results.

Considering the commercial application of OSCs, the stability of materials has become an essential parameter. Therefore, we compared the stabilities of the ITIC-2Cl- δ , ITIC-2Cl- m , and ITIC-2Cl- γ -based devices, as shown in Figure 7. The V_{OC} of the three acceptor-based devices have almost no change during the course of the lifetime test. The main differences between the three acceptor-based devices lie with J_{SC} and FF. Figure 7A shows that the J_{SC} of the ITIC-2Cl- δ -based device drops by 8.0% and that of the ITIC-2Cl- m -based device drops by 13.5% over 56 days, whereas the ITIC-2Cl- γ -based device shows only a 5.3% J_{SC} decline. On the other hand, the FF of the ITIC-2Cl- γ -based device is highly stable over 70% with almost no change, whereas the ITIC-2Cl- δ and ITIC-2Cl- m -based devices show a significant decline in FF. The ITIC-2Cl- γ -based device shows the most stable J_{SC} and FF, corresponding to the stable 3D rectangle-like interpenetrating network structure, whereas the ITIC-2Cl- m -based device shows the worst stability, which might be caused by the impure phase separation of the mixture. These results indicate that the use of the mixture as the active layer would reduce the stability of the device; the different molecular configurations would affect the stability of the device, whereas the 3D rectangle-like interpenetrating network structure could be used to prepare highly stable OSC devices to further meet the commercial needs of OSCs. We also characterized the photo-stability under illumination and heating at 80°C in N_2 atmosphere for 200 h, which are shown in Figures S12 and S13, respectively. The results match well with the stabilities of unencapsulated devices stored in a glove box, which we discussed above.

We have tried other donor materials to prove that the law of PCE is universal. We chose another polymer PBDB-T2Cl as donor pairing with the three acceptors ITIC-2Cl- γ , ITIC-2Cl- δ , and ITIC-2Cl- m . The J - V curves of devices using different NFAs with PBDB-T2Cl and EQE curves of the corresponding photovoltaic devices are shown in Figure S14. The corresponding photovoltaic parameters are shown in Table S2. The PBDB-T2Cl: ITIC-2Cl- γ -based device presents the highest V_{OC} of 0.92 V, J_{SC} of 18.79 mA cm^{-2} , and FF of 65.10%, leading to the highest PCE of 11.25%, and the PBDB-T2Cl: ITIC-2Cl- δ -based device presents a V_{OC} of 0.90 V, J_{SC} of 17.93 mA cm^{-2} , and FF of 62.29%, leading to an inferior PCE of 10.02%,

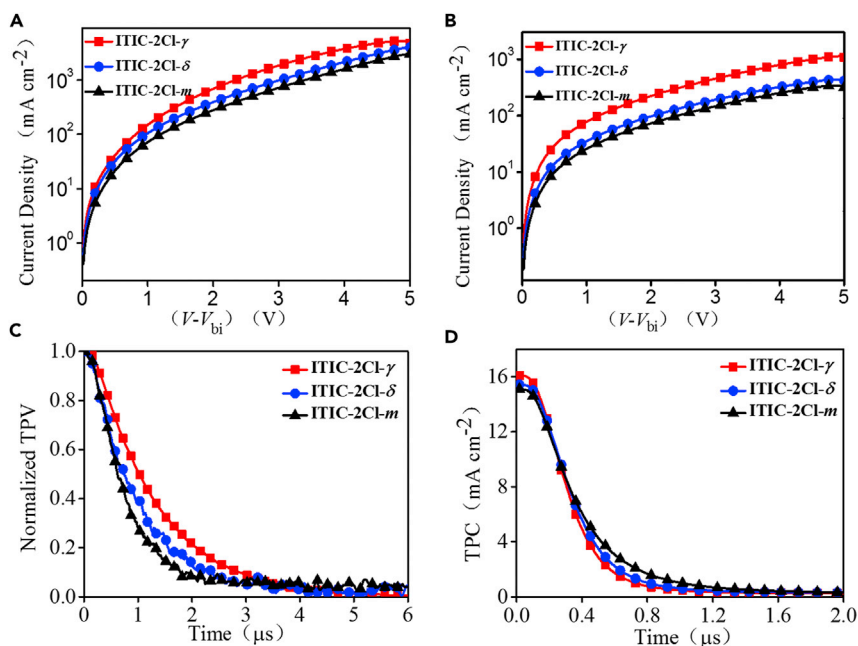


Figure 6. Device Performances Based on ITIC-2Cl- δ , ITIC-2Cl- m , and ITIC-2Cl- γ

(A) Double logarithmic plots of the current density (J) versus voltage (V) curves for the hole-only devices.

(B) Electron-only ITIC-2Cl- δ , ITIC-2Cl- m , and ITIC-2Cl- γ -based devices.

(C) Normalized transient photovoltage (TPV) of devices.

(D) Transient photocurrent of OSC devices.

Also see Table S1.

However, the lowest PCE of 9.41% with a V_{OC} of 0.90 V, J_{SC} of 17.44 mA cm⁻², and FF of 59.85% was observed in the PBDB-T2Cl: ITIC-2Cl- m -based device. The law is consistent with the previous devices based on PBDB-T2F with different NFAs. In addition, The calculated J_{cal} of ITIC-2Cl- δ , ITIC-2Cl- m , and ITIC-2Cl- γ devices based on the EQE curves are 17.15 mA cm⁻², 16.70 mA cm⁻², and 17.88 mA cm⁻², respectively, which matches well with the J_{SC} values from the above J - V test curves based on PBDB-T2Cl: NFAs devices.

The grazing-incidence wide angle X-ray scattering (GIWAXS) was measured to characterize the orientation and stacking of molecules in the blend films (Figure S15). As shown in Figures S15A–S15C, the molecules all present the face-on stacking pattern in the blend films. The intensity of ITIC-2Cl- γ -blend film is the highest, as shown in Figure S15E, the peak at 1.77 Å⁻¹ corresponding to the π - π stacking of 3.55 Å, whereas the peak at 1.74 Å⁻¹ of ITIC-2Cl- δ -blend film shows the π - π stacking of 3.61 Å. The shorter π - π stacking the ITIC-2Cl- γ blend film is consistent with single crystal data, which may prove the correlation between the structure in single crystal and the blend films from sideways.

The charge transport properties of three NFAs were evaluated by fabricating top-gate/bottom-contact organic thin-film transistors (OTFTs). The device performance parameters of the top-gate OTFTs fabricated under optimal conditions are summarized in Table S3, and the corresponding representative I–V curves are plotted in Figure S16. In detail, ITIC-2Cl- γ OTFTs show an average electron mobility (μ_e) of 0.091 cm² V⁻¹ s⁻¹ and an average hole mobility (μ_h) of 0.010 cm² V⁻¹ s⁻¹, which was higher than the average electron mobility (μ_e) of 0.041 cm² V⁻¹ s⁻¹ and the average hole mobility (μ_h) of 0.0038 cm² V⁻¹ s⁻¹ to ITIC-2Cl- δ OTFTs. The results match well with the electron and hole mobilities measured by the SCLC method in Figure 6 and Table 1, which could prove the correlation between the packing mode in single crystal and the blend films indirectly. In addition, the higher electron mobility of three NFA OTFTs than hole mobility indicated the three molecules are N-type materials, corresponding to the properties of electron acceptors (Li et al., 2018a, 2018b, 2018c, 2018d; Gao et al., 2018a, 2018b).

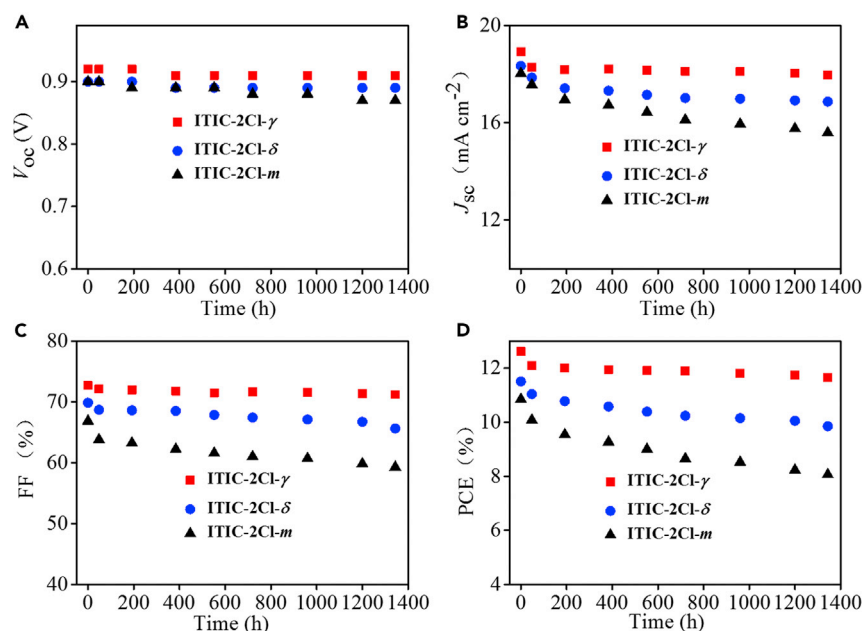


Figure 7. The Stabilities of Unencapsulated Devices Stored in a Glove Box

(A) The relationship between open-circuit voltage (V_{OC}) and time.

(B) The relationship between short-circuit current density (J_{SC}) and time.

(C) The relationship between fill factor (FF) and time.

(D) The relationship between power conversion efficiencies (PCEs) and time.

Also see Figures S12 and S13.

Conclusion

Two isomer-free NFAs ITIC-2Cl- δ and ITIC-2Cl- γ were successfully synthesized by precise chlorine atom positioning at the IC end groups. The single-crystal structures of ITIC-2Cl- δ and ITIC-2Cl- γ indicate that the different positions of the chlorine atoms significantly influence the molecular orientation and packing. Compared with ITIC-2Cl- δ , ITIC-2Cl- γ shows a better molecular planarity and a closer π - π interaction distance. The latter exhibits a 3D interpenetrating network structure, whereas only a linear stacked structure is observed for ITIC-2Cl- δ . The different positions of the chlorine atom on the end group can affect not only the absorption spectra but also the energy levels. After blending with the donor polymer PBDB-T2F, the ITIC-2Cl- γ -based device shows the highest PCE of 13.03%, which benefits from a higher J_{SC} (18.94 mA cm^{-2}) and FF (74.07%), whereas the lowest PCE (10.85%) is obtained by the ITIC-2Cl- m -based device. In addition, the most stable performance is observed by the ITIC-2Cl- γ -based device, which will be conducive to the commercial application of OSCs. These results demonstrate that the position of the chlorine atom on the end group has a great impact on the performance of the acceptor-based device. The 3D interpenetrating charge carrier transport or more ideal isotropic transmission properties in fullerene acceptors may be a strategy to design high-performance NFAs to further improve PCE and device stability for commercial application of OSCs.

Limitations of the Study

In this study, the single-crystal structures of two NFAs were investigated to analyze the effect of different chlorine atom positions on device performance. However, owing to the limitation of experimental condition, the stacked structure of these molecules in the blend film could not be observed.

METHODS

All methods can be found in the accompanying Transparent Methods supplemental file.

SUPPLEMENTAL INFORMATION

Supplemental Information can be found online at <https://doi.org/10.1016/j.isci.2019.06.033>.

ACKNOWLEDGMENTS

This work was financially supported by the National Natural Science Foundation of China (21733005, 51773087, 51603100), Shenzhen Fundamental Research program (JCYJ20170817111214740, KQJSCX20180319114442157), and Shenzhen Nobel Prize Scientists Laboratory Project (C17783101).

AUTHOR CONTRIBUTIONS

H.L. carried out the most experiments and materials synthesis; H.C. finished the device fabrication; J.Z., X.C., and Z.X. finished the single-crystal measurements; H.L. and F.H. wrote the manuscript with input from the other co-authors; F.H. supervised the project.

DECLARATION OF INTERESTS

The authors declare no competing financial interests.

Received: December 13, 2018

Revised: March 25, 2019

Accepted: June 22, 2019

Published: July 26, 2019

REFERENCES

- Aldrich, T.J., Matta, M., Zhu, W., Swick, S.M., Stern, C.L., Schatz, G.C., Facchetti, A., Melkonyan, F.S., and Marks, T.J. (2019). Fluorination effects on indacenodithienothiophene acceptor packing and electronic structure, end-group redistribution, and solar cell photovoltaic response. *J. Am. Chem. Soc.* **141**, 3274–3287.
- Cai, K., Xie, J., Zhang, D., Shi, W., Yan, Q., and Zhao, D. (2018). Concurrent cooperative J-aggregates and anticooperative H-aggregates. *J. Am. Chem. Soc.* **140**, 5764–5773.
- Cha, H., Wu, J., Wadsworth, A., Nagitta, J., Limbu, S., Pont, S., Li, Z., Searle, J., Wyatt, M.F., Baran, D., et al. (2017). An efficient, “Burn in” free organic solar cell employing a nonfullerene electron acceptor. *Adv. Mater.* **29**, 1701156.
- Chao, P., Wang, H., Mo, D., Meng, H., Chen, W., and He, F. (2018). Synergistic effects of chlorination and a fully two-dimensional side-chain design on molecular energy level modulation toward non-fullerene photovoltaics. *J. Mater. Chem. A* **6**, 2942–2951.
- Che, X., Li, Y., Qu, Y., and Forrest, S.R. (2018). High fabrication yield organic tandem photovoltaics combining vacuum- and solution-processed subcells with 15% efficiency. *Nat. Energy* **3**, 422–427.
- Chen, Y., Liu, T., Hu, H., Ma, T., Lai, J.Y.L., Zhang, J., Ade, H., and Yan, H. (2018). Modulation of end groups for low-bandgap nonfullerene acceptors enabling high-performance organic solar cells. *Adv. Energy Mater.* **8**, 1801203.
- Cheng, P., Li, G., Zhan, X., and Yang, Y. (2018). Next-generation organic photovoltaics based on non-fullerene acceptors. *Nat. Photonics* **12**, 131–142.
- Cui, Y., Yao, H., Gao, B., Qin, Y., Zhang, S., Yang, B., He, C., Xu, B., and Hou, J. (2017a). Fine-tuned photoactive and interconnection layers for achieving over 13% efficiency in a fullerene-free tandem organic solar cell. *J. Am. Chem. Soc.* **139**, 7302–7309.
- Cui, Y., Yang, C., Yao, H., Zhu, J., Wang, Y., Jia, G., Gao, F., and Hou, J. (2017b). Efficient semitransparent organic solar cells with tunable color enabled by an ultralow-bandgap nonfullerene acceptor. *Adv. Mater.* **29**, 1703080.
- Fan, Q., Zhu, Q., Xu, Z., Su, W., Chen, J., Wu, J., Guo, X., Ma, W., Zhang, M., and Li, Y. (2018a). Chlorine substituted 2D-conjugated polymer for high-performance polymer solar cells with 13.1% efficiency via toluene processing. *Nano Energy* **48**, 413–420.
- Fan, Q., Su, W., Wang, Y., Guo, B., Jiang, Y., Guo, X., Liu, F., Russell, T.P., Zhang, M., and Li, Y. (2018b). Synergistic effect of fluorination on both donor and acceptor materials for high performance non-fullerene polymer solar cells with 13.5% efficiency. *Sci. China Chem.* **61**, 531–537.
- Fei, Z., Eisner, F.D., Jiao, X., Azzouzi, M., Rohr, J.A., Han, Y., Shahid, M., Chesman, A.S.R., Easton, C.D., McNeill, C.R., et al. (2018). An alkylated indacenodithieno[3,2-b]thiophene-based nonfullerene acceptor with high crystallinity exhibiting single junction solar cell efficiencies greater than 13% with low voltage losses. *Adv. Mater.* **30**, 1705209.
- Feng, S., Zhang, C., Liu, Y., Bi, Z., Zhang, Z., Xu, X., Ma, W., and Bo, Z. (2017). Fused-ring acceptors with asymmetric side chains for high-performance thick-film organic solar cells. *Adv. Mater.* **29**, 1703527.
- Gao, W., Zhang, M., Liu, T., Ming, R., An, Q., Wu, K., Xie, D., Luo, Z., Zhong, C., Liu, F., et al. (2018a). Asymmetrical ladder-type donor-induced polar small molecule acceptor to promote fill factors approaching 77% for high-performance nonfullerene polymer solar cells. *Adv. Mater.* **30**, 1800052.
- Gao, B., Yao, H., Jang, B., Zhu, J., Yu, R., Cui, Y., Wang, F., Hou, J., Woo, H., and Hou, J. (2018b). The crucial role of intermolecular π - π interactions in A–D–A-type electron acceptors and their effective modulation. *J. Mater. Chem. A* **6**, 2664–2670.
- He, Z., Xiao, B., Liu, F., Wu, H., Yang, Y., Xiao, S., Wang, C., Russell, T.P., and Cao, Y. (2015). Single-junction polymer solar cells with high efficiency and photovoltage. *Nat. Photonics* **9**, 174–179.
- Hestand, N.J., and Spano, F.C. (2017). Molecular aggregate photophysics beyond the Kasha Model: novel design principles for organic materials. *Acc. Chem. Res.* **50**, 341–350.
- Holliday, S., Ashraf, R.S., Wadsworth, A., Baran, D., Yousaf, S.A., Nielsen, C.B., Tan, C.H., Dimitrov, S.D., Shang, Z., Gasparini, N., and Alamoudi, M. (2016). High-efficiency and air-stable P3HT-based polymer solar cells with a new non-fullerene acceptor. *Nat. Commun.* **7**, 11585.
- Hou, J., Inganäs, O., Friend, R.H., and Gao, F. (2018). Organic solar cells based on non-fullerene acceptors. *Nat. Mater.* **17**, 119–128.
- Kan, B., Feng, H., Wan, X., Liu, F., Ke, X., Wang, Y., Wang, Y., Zhang, H., Li, C., Hou, J., and Chen, Y. (2017a). Small-molecule acceptor based on the heptacyclic benzodi(cyclopentadithiophene) unit for highly efficient nonfullerene organic solar cells. *J. Am. Chem. Soc.* **139**, 4929–4934.
- Kan, B., Zhang, J., Liu, F., Wan, X., Li, C., Ke, X., Wang, Y., Feng, H., Zhang, Y., Long, G., et al. (2017b). Fine-tuning the energy levels of a nonfullerene small-molecule acceptor to achieve a high short-circuit current and a power conversion efficiency over 12% in organic solar cells. *Adv. Mater.* **30**, 1704904.
- Li, H., Earmme, T., Ren, G., Saeki, A., Yoshikawa, S., Murari, N.M., Subramanian, S., Crane, M.J., Seki, S., and Jenekhe, S.A. (2014). Beyond fullerenes: design of nonfullerene acceptors for efficient organic photovoltaics. *J. Am. Chem. Soc.* **136**, 14589–14597.
- Li, Y., Lin, J.D., Che, X., Qu, Y., Liu, F., Liao, L.S., and Forrest, S.R. (2017). High efficiency near-infrared and semitransparent non-fullerene acceptor organic photovoltaic cells. *J. Am. Chem. Soc.* **139**, 17114–17119.

- Li, H., Xiao, Z., Ding, L., and Wang, J. (2018a). Thermostable single-junction organic solar cells with a power conversion efficiency of 14.62%. *Sci. Bull.* **63**, 340–342.
- Li, S., Ye, L., Zhao, W., Yan, H., Yang, B., Liu, D., Li, W., Ade, H., and Hou, J. (2018b). A wide band gap polymer with a deep highest occupied molecular orbital level enables 14.2% efficiency in polymer solar cells. *J. Am. Chem. Soc.* **30**, 1707508.
- Li, W., Ye, L., Li, S., Yao, H., Ade, H., and Hou, J. (2018c). A high-efficiency organic solar cell enabled by the strong intramolecular electron push-pull effect of the nonfullerene acceptor. *Adv. Mater.* **30**, 1707170.
- Li, S., Zhan, L., Zhao, W., Zhang, S., Ali, B., Fu, Z., Lau, T., Liu, X., Shi, M., Li, C., et al. (2018d). Revealing the effects of molecular packing on the performances of polymer solar cells based on A–D–C–D–A type non-fullerene acceptors. *J. Mater. Chem. A* **6**, 12132–12141.
- Lin, Y., Wang, J., Zhang, Z.G., Bai, H., Li, Y., Zhu, D., and Zhan, X. (2015). An electron acceptor challenging fullerenes for efficient polymer solar cells. *Adv. Mater.* **27**, 1170–1174.
- Lin, Y., He, Q., Zhao, F., Huo, L., Mai, J., Lu, X., Su, C.J., Li, T., Wang, J., Zhu, J., et al. (2016). A facile planar fused-ring electron acceptor for as-cast polymer solar cells with 8.71% efficiency. *J. Am. Chem. Soc.* **138**, 2973–2976.
- Liu, Y., Zhao, J., Li, Z., Mu, C., Ma, W., Hu, H., Jiang, K., Lin, H., Ade, H., and Yan, H. (2014). Aggregation and morphology control enables multiple cases of high-efficiency polymer solar cells. *Nat. Commun.* **5**, 5293.
- Mo, D., Wang, H., Chen, H., Qu, S., Chao, P., Yang, Z., Tian, L., Su, Y.-A., Gao, Y., Yang, B., et al. (2017). Chlorination of low-band-gap polymers: toward high-performance polymer solar cells. *Chem. Mater.* **29**, 2819–2830.
- Nielsen, C.B., Holliday, S., Chen, H.Y., Cryer, S.J., and McCulloch, I. (2015). Non-fullerene electron acceptors for use in organic solar cells. *Acc. Chem. Res.* **48**, 2803–2812.
- Ouyang, X., Peng, R., Ai, L., Zhang, X., and Ge, Z. (2015). Efficient polymer solar cells employing a non-conjugated small-molecule electrolyte. *Nat. Photonics* **9**, 520–524.
- Qu, J., Chen, H., Zhou, J., Lai, H., Liu, T., Chao, P., Li, D., Xie, Z., He, F., and Ma, Y. (2018). Chlorine atom-induced molecular interlocked network in a non-fullerene acceptor. *ACS Appl. Mater. Interfaces* **10**, 39992–40000.
- Shi, X., Zuo, L., Jo, S.B., Gao, K., Lin, F., Liu, F., and Jen, A.K.Y. (2017). Design of a highly crystalline low-band gap fused-ring electron acceptor for high-efficiency solar cells with low energy loss. *Chem. Mater.* **29**, 8369–8376.
- Sun, J., Ma, X., Zhang, Z., Yu, J., Zhou, J., Yin, X., Yang, L., Geng, R., Zhu, R., Zhang, F., and Tang, W. (2018). Dithieno[3,2-b:2',3'-d]pyrrol fused nonfullerene acceptors enabling over 13% efficiency for organic solar cells. *Adv. Mater.* **30**, 1707150.
- Swick, S.M., Zhu, W., Matta, M., Aldrich, T.J., Harbuzaru, A., Lopez Navarrete, J.T., Ponce Ortiz, R., Kohlstedt, K.L., Schatz, G.C., Facchetti, A., and Marks, T.N. (2018). Closely packed, low reorganization energy pi-extended postfullerene acceptors for efficient polymer solar cells. *Proc. Natl. Acad. Sci. U S A* **115**, E8341–E8348.
- Wadsworth, A., Moser, M., Marks, A., Little, M.S., Gasparini, N., Brabec, C.J., Baran, D., and McCulloch, I. (2018). Critical review of the molecular design progress in non-fullerene electron acceptors towards commercially viable organic solar cells. *Chem. Soc. Rev.* <https://doi.org/10.1039/c7cs00892a>.
- Wang, J., Wang, W., Wang, X., Wu, Y., Zhang, Q., Yan, C., Ma, W., You, W., and Zhan, X. (2017). Enhancing performance of nonfullerene acceptors via side-chain conjugation strategy. *Adv. Mater.* **29**, 1702125.
- Wang, Y., Zhang, Y., Qiu, N., Feng, H., Gao, H., Kan, B., Ma, Y., Li, C., Wan, X., and Chen, Y. (2018a). A halogenation strategy for over 12% efficiency nonfullerene organic solar cells. *Adv. Energy Mater.* **8**, 1702870.
- Wang, J., Zhang, J., Xiao, Y., Xiao, T., Zhu, R., Yan, C., Fu, Y., Lu, G., Lu, X., Marder, S.R., and Zhan, X. (2018b). Effect of isomerization on high-performance nonfullerene electron acceptors. *J. Am. Chem. Soc.* **140**, 9140–9147.
- Wang, H., Cao, J., Yu, J., Zhang, Z., Geng, R., Yang, L., and Tang, W. (2019). Molecular engineering of central fused-ring cores of non-fullerene acceptors for high-efficiency organic solar cells. *J. Mater. Chem. A* **7**, 4313–4333.
- Xiao, Z., Jia, X., Li, D., Wang, S., Geng, X., Liu, F., Chen, J., Yang, S., Russell, T.P., and Ding, L. (2017). 26 mA cm⁻² Jsc from organic solar cells with a low-bandgap nonfullerene acceptor. *Sci. Bull.* **62**, 1494–1496.
- Xie, D., Liu, T., Gao, W., Zhong, C., Huo, L., Luo, Z., Wu, K., Xiong, W., Liu, F., Sun, Y., and Yang, C. (2017). A novel thiophene-fused ending group enabling an excellent small molecule acceptor for high-performance fullerene-free polymer solar cells with 11.8% efficiency. *Solar RRL* **1**, 1700044.
- Xie, Y., Yang, F., Li, Y., Uddin, M.A., Bi, P., Fan, B., Cai, Y., Hao, X., Woo, H.Y., Li, W., et al. (2018). Morphology control enables efficient ternary organic solar cells. *Adv. Mater.* **30**, 1803045.
- Xu, X., Yu, T., Bi, Z., Ma, W., Li, Y., and Peng, Q. (2018). Realizing over 13% efficiency in green-solvent-processed nonfullerene organic solar cells enabled by 1,3,4-Thiadiazole-Based Wide-Bandgap copolymers. *Adv. Mater.* **30**, 1703973.
- Yan, D., Liu, W., Yao, J., and Zhan, C. (2018). Fused-ring nonfullerene acceptor forming interpenetrating J-architecture for fullerene-free polymer solar cells. *Adv. Energy Mater.* **8**, 1800204.
- Yang, Y., Zhang, Z.G., Bin, H., Chen, S., Gao, L., Xue, L., Yang, C., and Li, Y. (2016). Side-chain isomerization on an n-type organic semiconductor ITIC acceptor makes 11.77% high efficiency polymer solar cells. *J. Am. Chem. Soc.* **138**, 15011–15018.
- Yang, F., Li, C., Lai, W., Zhang, A., Huang, H., and Li, W. (2017). Halogenated conjugated molecules for ambipolar field-effect transistors and non-fullerene organic solar cells. *Mater. Chem. Front.* **1**, 1389–1395.
- Yao, Z., Liao, X., Gao, K., Lin, F., Xu, X., Shi, X., Zuo, L., Liu, F., Chen, Y., and Jen, A.K. (2018). Dithienopicenocarbazole-based acceptors for efficient organic solar cells with optoelectronic response over 1000 nm and an extremely low energy loss. *J. Am. Chem. Soc.* **140**, 2054–2057.
- Zhang, H., Yao, H., Hou, J., Zhu, J., Zhang, J., Li, W., Yu, R., Gao, B., Zhang, S., and Hou, J. (2018a). Over 14% efficiency in organic solar cells enabled by chlorinated nonfullerene small-molecule acceptors. *Adv. Mater.* **30**, 1800868.
- Zhang, Y., Kan, B., Sun, Y., Wang, Y., Xia, R., Ke, X., Yi, Y.Q., Li, C., Yip, H.L., Wan, X., et al. (2018b). Nonfullerene tandem organic solar cells with high performance of 14.11. *Adv. Mater.* **30**, 1707508.
- Zhang, Y., Yao, H., Zhang, S., Qin, Y., Zhang, J., Yang, L., Li, W., Wei, Z., Gao, F., and Hou, J. (2018c). Fluorination vs. chlorination: a case study on high performance organic photovoltaic materials. *Sci. China Chem.* **61**, 1328–1337.
- Zhang, S., Qin, Y., Zhu, J., and Hou, J. (2018d). Over 14% efficiency in polymer solar cells enabled by a chlorinated polymer donor. *Adv. Mater.* **30**, 1800868.
- Zhao, J., Li, Y., Yang, G., Jiang, K., Lin, H., Ade, H., Ma, W., and Yan, H. (2016). Efficient organic solar cells processed from hydrocarbon solvents. *Nat. Energy* **1**, 15027.
- Zhao, F., Dai, S., Wu, Y., Zhang, Q., Wang, J., Jiang, L., Ling, Q., Wei, Z., Ma, W., You, W., et al. (2017). Single-junction binary-blend nonfullerene polymer solar cells with 12.1% efficiency. *Adv. Mater.* **29**, 1700144.

ISCI, Volume 17

Supplemental Information

**Isomer-free: Precise Positioning of Chlorine-Induced
Interpenetrating Charge Transfer
for Elevated Solar Conversion**

Hanjian Lai, Hui Chen, Jiadong Zhou, Jianfei Qu, Pengjie Chao, Tao Liu, Xiaoyong Chang, Nan Zheng, Zengqi Xie, and Feng He

Supplemental Information

Isomer-free: Precise Positioning of Chlorine Induced Interpenetrating Charge Transfer for Elevated Solar Conversion

Hanjian Lai^{1, 2, †}, Hui Chen^{1, †}, Jiadong Zhou^{3, †}, Jianfei Qu¹, Pengjie Chao¹, Tao Liu¹, Xiaoyong Chang¹, Nan Zheng³, Zengqi Xie³, and Feng He^{1, 4 *}

¹Department of Chemistry and Shenzhen Grubbs Institute, Southern University of Science and Technology, Shenzhen 518055, China.

²School of Chemistry and Chemical Engineering, Harbin Institute of Technology, Harbin, 150001, China.

³Institute of Polymer Optoelectronic Materials and Devices, State Key Laboratory of Luminescent Materials and Devices, South China University of Technology, Guangzhou 510640, China.

⁴Lead Contact

*Corresponding author

E-mail addresses: hef@sustech.edu.cn (F. He)

† These authors contributed equally to this work.

Transparent Methods

Instruments and characterization: ^1H NMR spectra were recorded on Bruker AV 400 MHz spectrometer in CDCl_3 with tetramethylsilane (TMS) as an internal standard. Preparative gel permeation chromatography purification was performed with a JAI LC-9104 recycling preparative high performance liquid chromatography, and the eluent was chloroform. Cyclic voltammetry (CV) measurements were performed on a CHI 660E potentiostat/galvanostat (Shanghai Chenhua Instrumental Co., Ltd. China) to determine the HOMO and LUMO levels of the polymers, in an acetonitrile solution of 0.1 mol L^{-1} tetrabutylammonium hexafluorophosphate ($[\text{n-Bu}_4\text{N}]^+ [\text{PF}_6]^-$) at a potential scan rate of 100 mV s^{-1} with an Ag/Ag^+ reference electrode and a platinum wire counter electrode under a argon atmosphere. Solution and film UV-Vis absorption spectra were recorded on a Shimadzu UV3600 spectrometer. Thermogravimetric analysis (TGA) plots were measured with a Discovery series instrument under a nitrogen atmosphere at heating and cooling rates of $10 \text{ }^\circ\text{C min}^{-1}$. Different scanning calorimetry (DSC) measurements were performed on a Discovery series thermal analyzer at a scanning rate of $10 \text{ }^\circ\text{C min}^{-1}$ in N_2 . Atom force microscopy (AFM) images were taken on a NanoScopeIIIa controller (Veeco Metrology Group/Digital Instruments, Santa Barbara, CA), using built-in software (version V6.13R1) to capture images. Transmission electron microscopy (TEM) images were acquired using a HITACHI H-7650 electron microscope operating at an acceleration voltage of 100 kV.

Fabrication and Characterization of OSCs: The fabrication and measurement methods of OSCs devices are as follows: After a thorough cleaning of the indium-tin oxide (ITO)-coated glass substrate with detergent, deionized water, acetone, and isopropyl alcohol under ultrasonication for 15 minutes each and subsequently dried in an oven for 1 minute at 80 °C under vacuum. The ITO glass substrates were treated with UV-ozone for 15 minutes and then the sol-gel-derived ZnO films were spin-coated onto the ITO substrates followed by thermal treatment at 200 °C for 30 min. The total concentration of the **PBDB-T2F**: Acceptor (1:1) blend solution for spin-coating was 20 mg mL⁻¹ with chlorobenzene as the processing solvent. The additive, 1, 8-diiodooctane (DIO) was added into solution 30 minutes before the spin-coating process. The blend was stirred at room temperature in the glove box overnight. The active layer was spin-coating at 2500 rpm for 45 s to get neat film. A 10 nm MoO₃ layer and a 100 nm Ag layer were subsequently evaporated through a shadow mask to define the active area of the devices. The integrated device structure is ITO/ZnO/**PBDB-T2F**: Acceptor/MoO₃/Ag. A solar simulator (Enlitech.Inc) with an AM 1.5G filter was used as a light source to produce an intensity of 100 mW cm⁻² for the illumination of the photovoltaic cells. The light intensity was calibrated by a 2 cm × 2 cm calibrated silicon solar cell with KG-3 visible color filter. A shadow mask with a single aperture (4.15 mm²) was placed onto the devices in order to accurately define the photoactive area. Steady-state current-voltage (*J-V*) curves were measured by a Keithley 2400 source-measurement unit under AM 1.5 G spectrum from a solar simulator (Enlitech. Inc)

calibrated by a silicon reference cell (Hamamatsu S1133 color, with KG-5 visible fiith). The relationship of J_{sc} to the light intensity were measured by steady-state current-voltage measurement, the light intensity was modulated by neutral density filters (NDF) with different values of optical density (OD). The external quantum efficiency (EQE) was measured by a solar cell photodetector responsibility measurement system (Enlitech. Inc).

Electron-only and hole-only devices fabrication: Electron-only devices were fabricated with the device structure of ITO/ZnO/**PBDB-T2F**: Acceptor/Ca/Al, while the hole-only devices were fabricated with the device structure of ITO/PEDOT: PSS/blends/MoO₃/Ag. The mobilities were determined by fitting the dark current to the model of a single carrier SCLC,^{1,2} which is described by the equation:

$$J = \frac{9}{8} \epsilon_0 \epsilon_r \mu_h \frac{V^2}{d^3}$$

where J is the current, μ_h is the zero-field mobility, ϵ_0 is the permittivity of free space, ϵ_r is the relative permittivity of the material, d is the thickness of the active layer, and V is the effective voltage.

Materials and Characterization: Compound **IDTT-CHO**, **IC-Cl-m** were synthesized according previously reported approaches.³⁻⁵ All the other chemicals were purchased as reagent grade from J&K, Energy, Macklin, and Sigma-Aldrich, and used without further purification. All solvents for reactions were freshly distilled immediately prior

to use.

Synthesis Compound ITIC-2Cl- δ : A mixture of **IDTT-CHO** (100 mg, 0.093 mmol), **IC-Cl- δ** (85 mg, 0.372 mmol), in chloroform/pyridine (20 ml/0.5 ml) was refluxed 24 hours under Argon. The reaction mixture was then cooled to room temperature and then extracted with chloroform. The organic layer was washed with brine and dried over MgSO₄. The crude product was purified by flash column chromatography with chloroform as eluent and further purified with cycling preparative HPLC to get the product (110 mg, 79%). ¹H NMR (400 MHz, CDCl₃) δ : 8.87 (s, 2H), 8.65 (s, 2H), 8.22 (s, 2H), 7.83-7.85 (d, 2H), 7.68-7.70 (dd, 2H), 7.64 (s, 2H), 7.13-7.22(m, 16H), 2.54-2.58(t, 8H), 1.57-1.63(m, 8H), 1.25-1.35(m, 24H), 0.84-0.94(m, 12H). ¹³C NMR (600 MHz, CDCl₃) δ : 186.86, 158.87, 155.77, 153.40, 147.72, 147.55, 143.84, 142.56, 141.84, 141.23, 139.64, 138.82, 138.61, 137.25, 137.00, 135.01, 134.55, 128.87, 127.85, 125.35, 124.71, 122.24, 118.62, 114.27, 114.19, 70.08, 63.24, 35.59, 31.69, 31.24, 29.17, 22.58, 14.08. MALDI-TOF-MS calcd for C₉₄H₈₀Cl₂N₄O₂S₄ (M⁺): 1494.4541, found: 1494.3944.

Synthesis Compound ITIC-2Cl-m: A mixture of **IDTT-CHO** (100 mg, 0.093 mmol), **IC-Cl-m** (85 mg, 0.372 mmol), in chloroform/pyridine (20 ml/0.5 ml) was refluxed 24 hours under Argon. The reaction mixture was then cooled to room temperature and then extracted with chloroform. The organic layer was washed with brine and dried over MgSO₄. The crude product was purified by flash column chromatography with chloroform as eluent and further purified with cycling preparative HPLC to get the

product (70 mg, 50%). ^1H NMR (400 MHz, CDCl_3) δ : 8.87 (s, 2H), 8.60-8.65 (m, 2H), 8.22-8.24 (d, 2H), 7.82-7.86 (m, 2H), 7.68-7.71 (m, 2H), 7.64-7.65 (d, 2H), 7.13-7.22(m, 16H), 2.55-2.59(t, 8H), 1.57-1.61(m, 8H), 1.26-1.35(m, 24H), 0.84-0.94(m, 12H). MALDI-TOF-MS calcd for $\text{C}_{94}\text{H}_{80}\text{Cl}_2\text{N}_4\text{O}_2\text{S}_4$ (M^+): 1494.4541, found: 1494.4077.

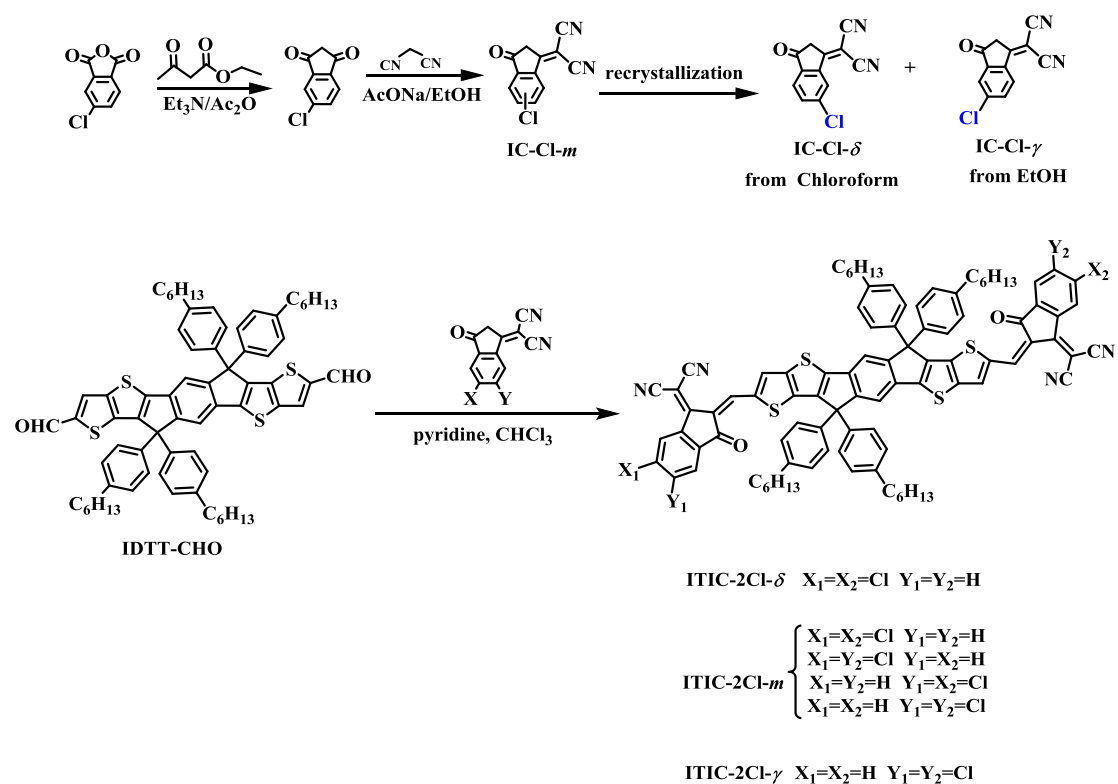
Synthesis Compound ITIC-2Cl- γ : A mixture of **IDTT-CHO** (100 mg, 0.093 mmol), **IC-Cl- γ** (85mg, 0.372 mmol), in chloroform/pyridine (20 ml/0.5 ml) was refluxed 24 hours under Argon. The reaction mixture was then cooled to room temperature and then extracted with chloroform. The organic layer was washed with brine and dried over MgSO_4 . The crude product was purified by flash column chromatography with chloroform as eluent and further purified with cycling preparative HPLC to get the product (97 mg, 67%). ^1H NMR (400 MHz, CDCl_3) δ : 8.87 (s, 2H), 8.60-8.63 (d, 2H), 8.24 (s, 2H), 7.85-7.86 (d, 2H), 7.68-7.71 (dd, 2H), 7.65 (s, 2H), 7.13-7.22(m, 16H), 2.55-2.59(t, 8H), 1.55-1.63(m, 8H), 1.26-1.37(m, 24H), 0.84-0.87(m, 12H). ^{13}C NMR (600 MHz, CDCl_3) δ : 186.73, 159.23, 155.77, 153.41, 147.71, 147.45, 143.87, 142.58, 141.24, 139.63, 138.82, 138.67, 138.31, 138.03, 137.21, 137.02, 134.94, 128.88, 127.85, 126.45, 123.88, 122.23, 118.63, 114.52, 114.38, 69.47, 63.25, 35.60, 31.69, 31.25, 29.18, 22.58, 14.08. MALDI-TOF-MS calcd for $\text{C}_{94}\text{H}_{80}\text{Cl}_2\text{N}_4\text{O}_2\text{S}_4$ (M^+): 1494.4541, found: 1494.3885.

Explaining A-and B-level alerts of ITIC-2Cl- δ : A full set of data was collected. However the very high angle data was dominated by noise [$I/\sigma(I) < 1.0$] and was omitted. This arbitrary theta limit is inappropriate for highly disordered structures. It would rule out all macromolecular structures. A limit on data / parameter ratio's that properly takes into account the number of restraints / constraints and the redundancy of the measurements would be more appropriate. Unfortunately the cifcheck routine does not do this.

Explaining B-level alerts of ITIC-2Cl- γ : We made several attempts to obtain better quality data for this structure. However, due to disorder, poor crystal quality etc. the R2 value is high. This structure is included for comparison with the other similar compounds. We are confident that the structural characterization is valid.

CCDC accession numbers: the accession number for the **ITIC-2Cl- γ** reported in this paper is 1884837; for the **ITIC-2Cl- δ** is 1884838; for the **IC-Cl- δ** is 1884839; and for the **IC-Cl- γ** is 1884840.

Supplemental Schemes



Scheme S1. The synthetic routes of **IC-Cl- δ** , and **IC-Cl- γ** , and the structures of **ITIC-2Cl-*m***, **ITIC-2Cl- δ** , and **ITIC-2Cl- γ** . Related to **Figure 1**.

Supplemental Figures

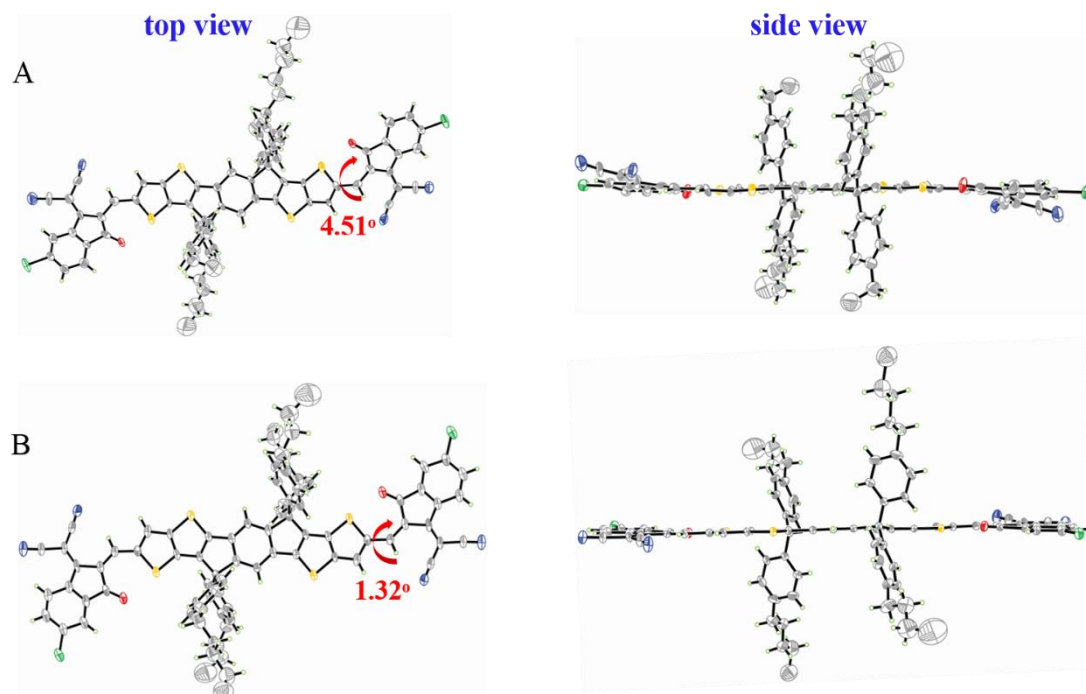


Figure S1. Crystal structures of (a) ITIC-2Cl- δ and (B) ITIC-2Cl- γ .

Related to **Figure 2**.

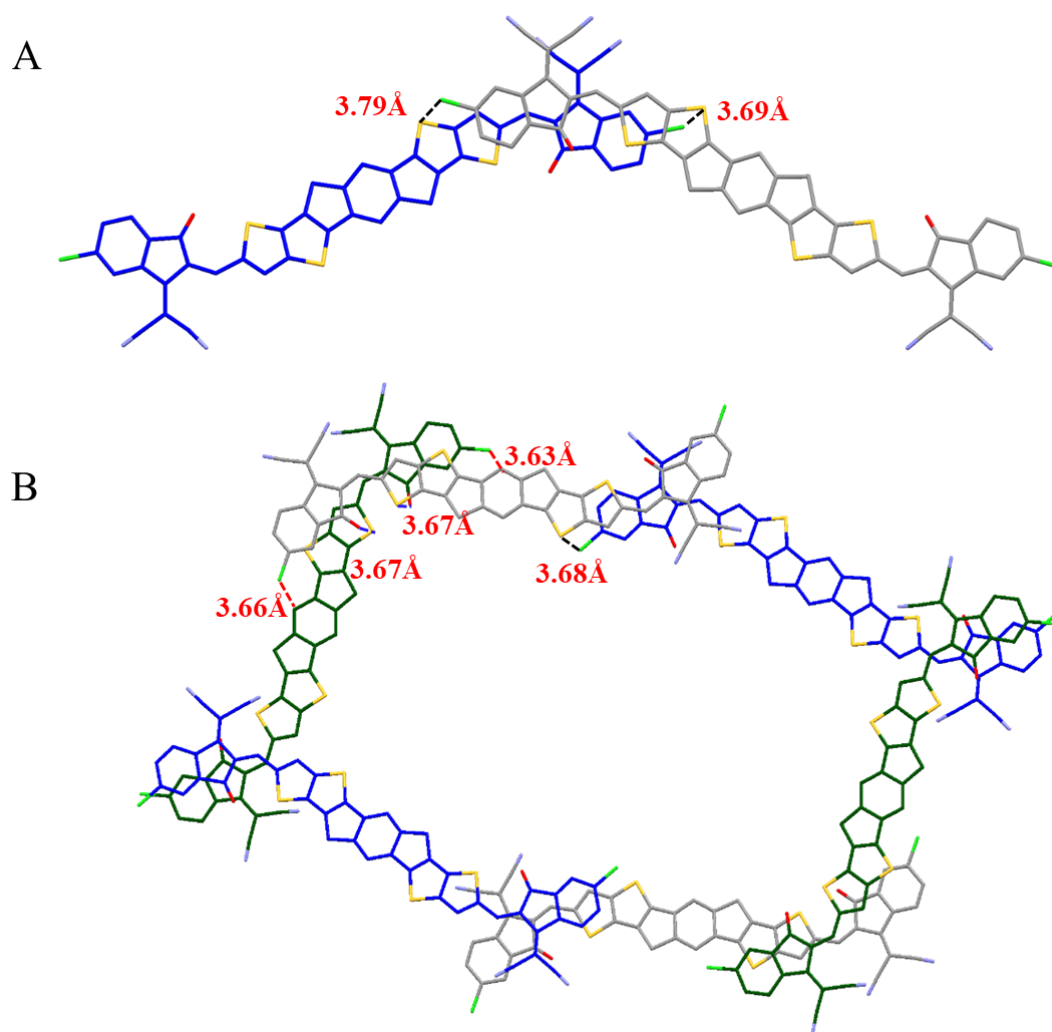


Figure S2. (A) Cl \cdots S (black) interaction of **ITIC-2Cl- δ** (B) Cl \cdots S (black), Cl \cdots π (red) and S \cdots O (blue) interaction of **ITIC-2Cl- γ** . (The hexyl benzene side chains were neglected for clarity). Related to **Figure 2**.

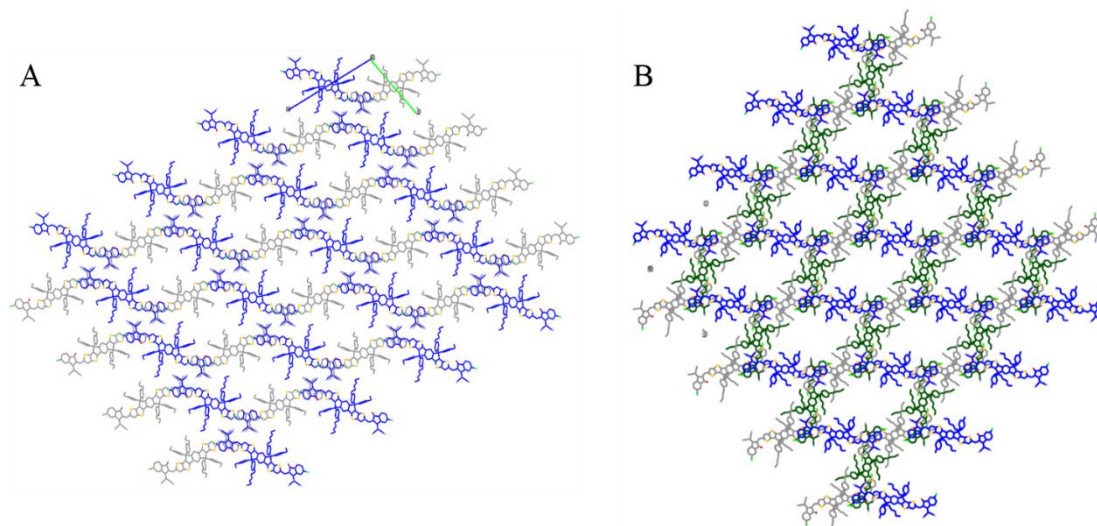


Figure S3. Crystal packing diagrams with hexyl benzene side chains for (A) ITIC-2Cl- δ , and (B) ITIC-2Cl- γ . Related to **Figure 3**.

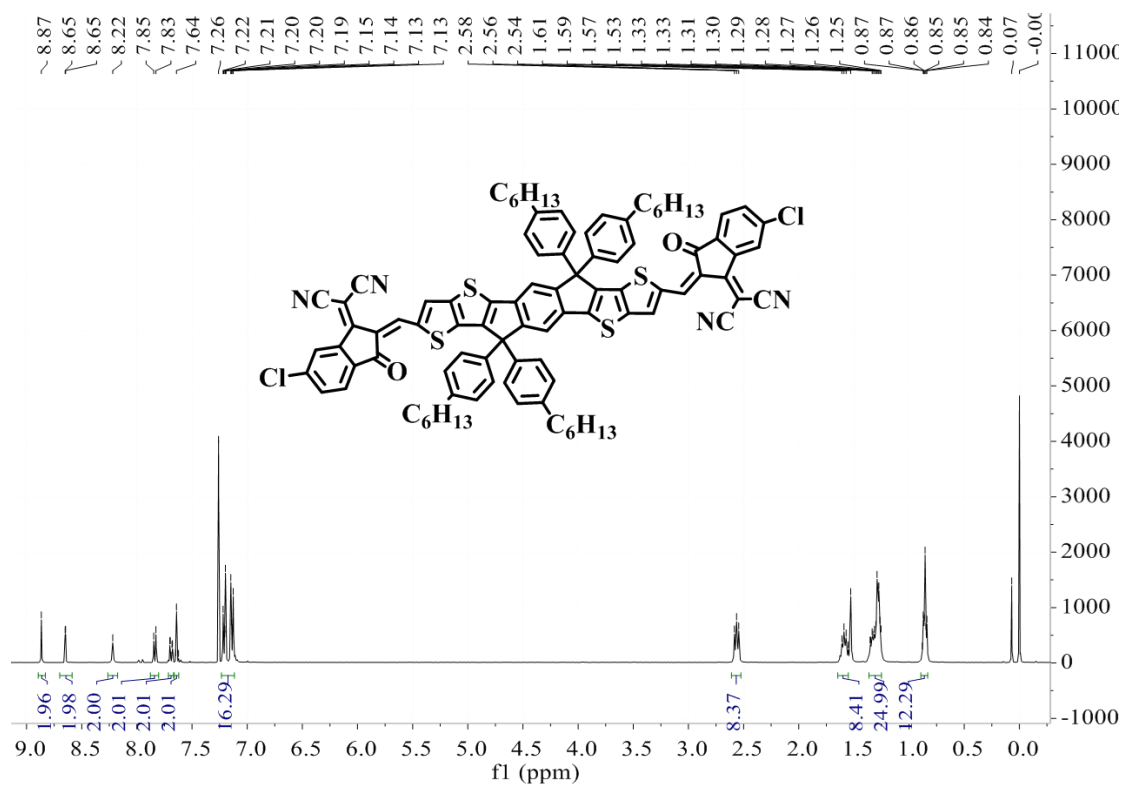


Figure S4. ^1H NMR of ITIC-2Cl- δ in CDCl_3 . Related to **Scheme 1**.

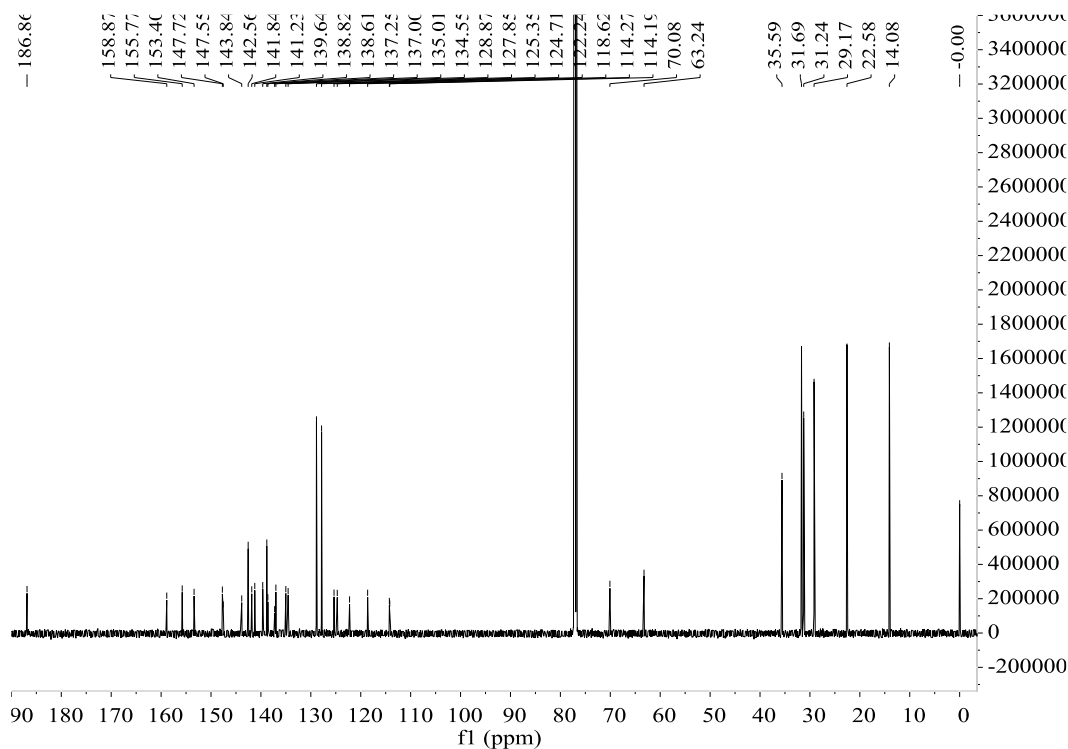


Figure S5. ^{13}C NMR of ITIC-2Cl- δ in CDCl_3 . Related to Scheme 1.

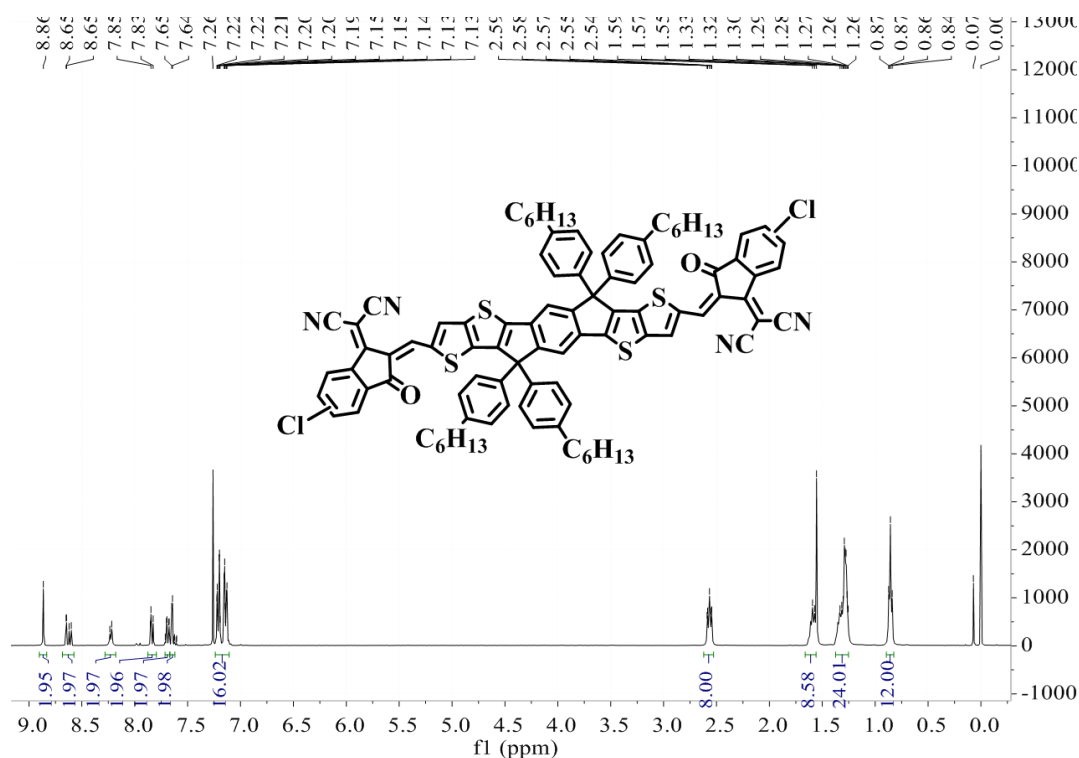


Figure S6. ^1H NMR of ITIC-2Cl- m in CDCl_3 . Related to Scheme 1.

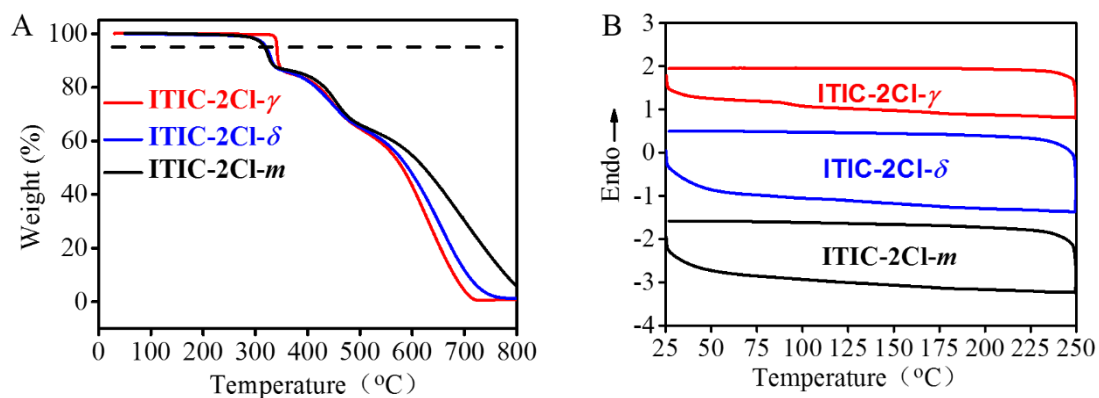


Figure S9. (A) Thermogravimetric analysis (TGA) results of **ITIC-2Cl- δ** , **ITIC-2Cl- m** and **ITIC-2Cl- γ** with a heating rate of $10\text{ }^{\circ}\text{C min}^{-1}$ under nitrogen purge. (B) Differential scanning calorimetry (DSC) results of **ITIC-2Cl- δ** , **ITIC-2Cl- m** and **ITIC-2Cl- γ** with heating and cooling rates of $10\text{ }^{\circ}\text{C min}^{-1}$ under nitrogen purge.

Related to **Figure 4**.

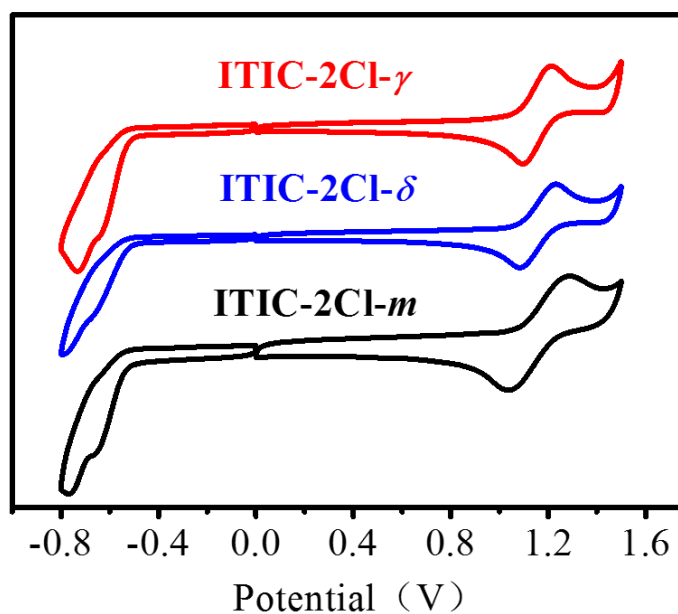


Figure S10. Cyclic voltammograms of **ITIC-2Cl- δ** , **ITIC-2Cl- m** and **ITIC-2Cl- γ** in dichloromethane with $(n\text{-Bu})_4\text{NPF}_6$ (0.1 M) as supporting electrolyte, Pt wire as counter electrode, and Ag/Ag^+ as reference electrode. Related to **Figure 4**.

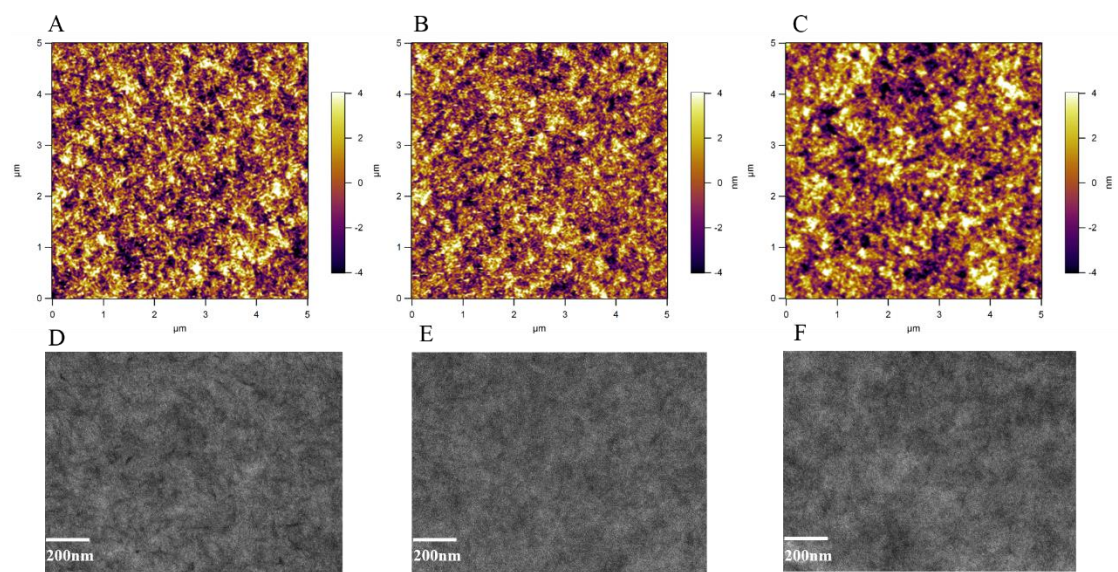


Figure S11. The AFM and TEM of ITIC-2Cl- δ (A, D), ITIC-2Cl-*m* (B, E) and ITIC-2Cl- γ (C, F). Related to **Figure 5**.

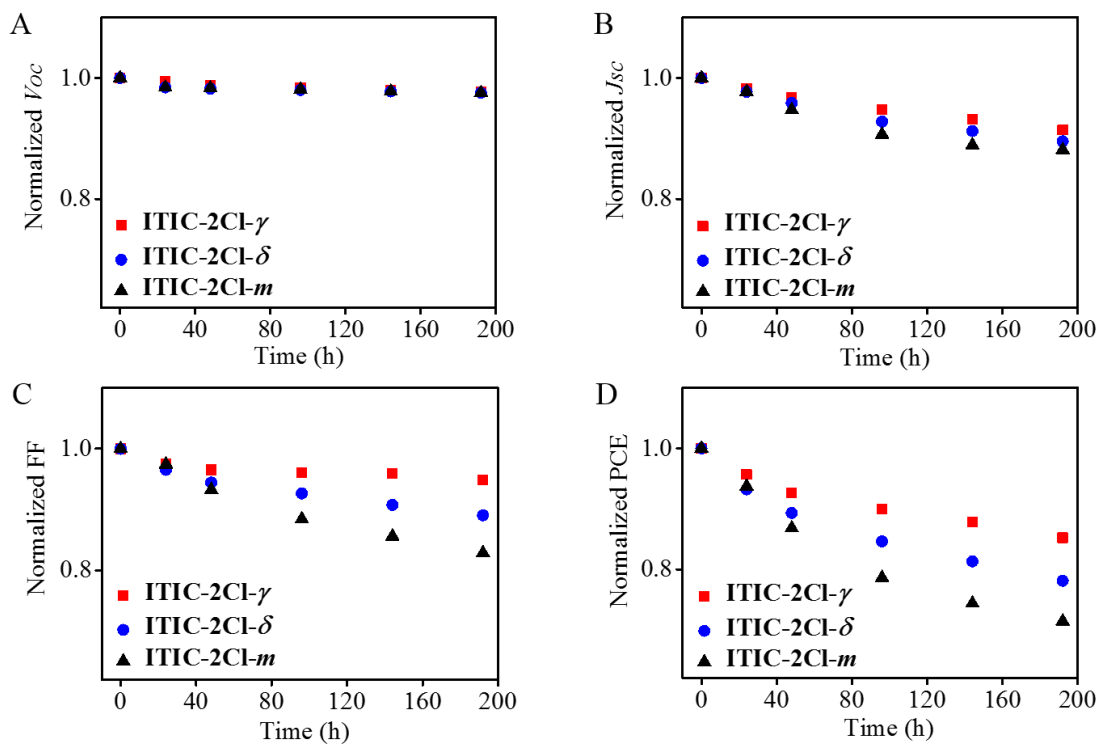


Figure S12. Stability test: evolution of photovoltaic parameters was determined under simulated illumination in N_2 atmosphere at room temperature. (A) Open-circuit voltage (V_{oc}). (B) Short-circuit current density (J_{sc}). (C) Fill factor (FF). (D) Power conversion efficiency (PCE). Related to **Figure 7**.

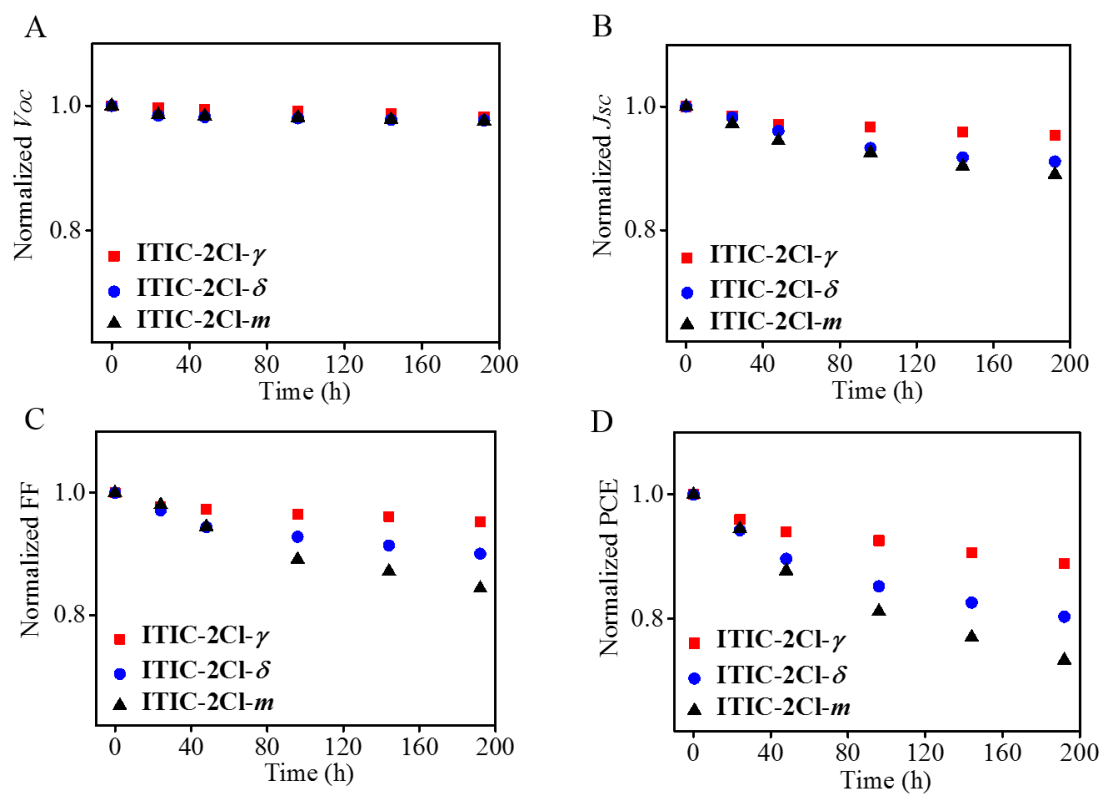


Figure S13. Stability test: evolution of photovoltaic parameters was determined at 80 °C in N₂ atmosphere. (A) Open-circuit voltage (V_{oc}). (B) Short-circuit current density (J_{sc}). (C) Fill factor (FF). (D) Power conversion efficiency (PCE).

Related to **Figure 7**.

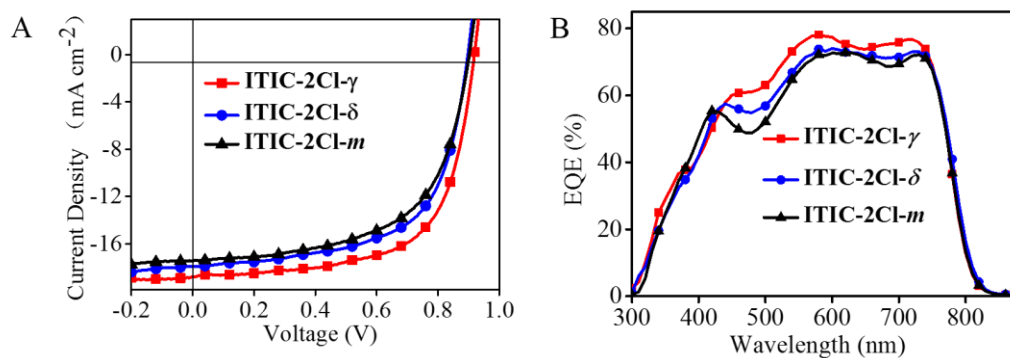


Figure S14. (A) J–V curves of devices using different NFAs with **PBDB-T2Cl**. (B) EQE curves of the corresponding photovoltaic devices. Related to **Figure 5**.

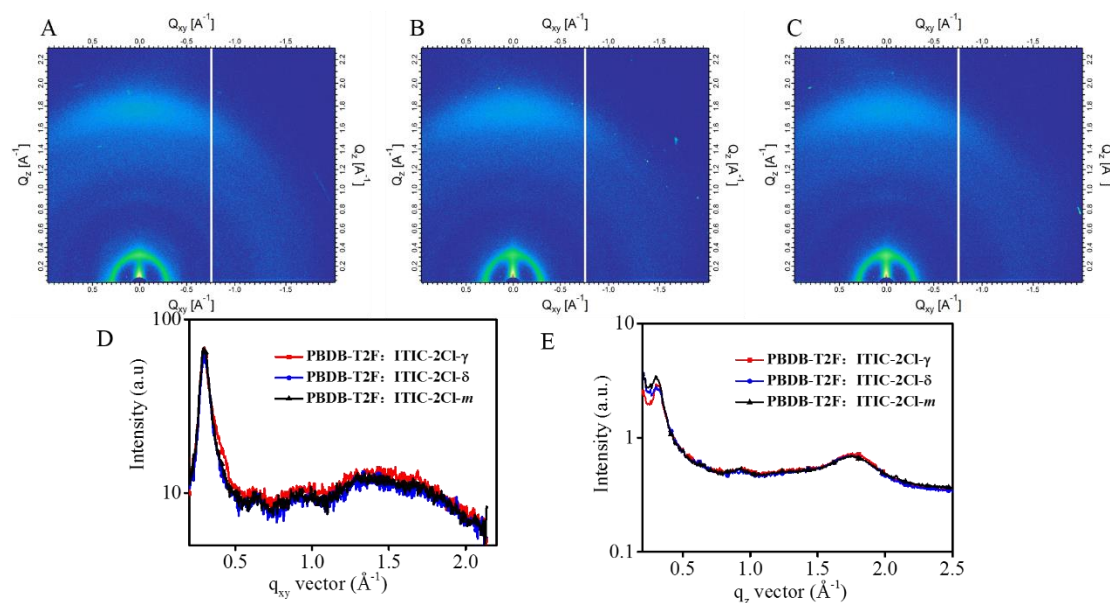


Figure S15. The GIWAXS of (A) **ITIC-2Cl- γ** -blend film, (B) **ITIC-2Cl- δ** -blend film and (C) **ITIC-2Cl- m** -blend film, (D, E) specific value of q_{xy} and q_z .

Related to **Figure 5**.

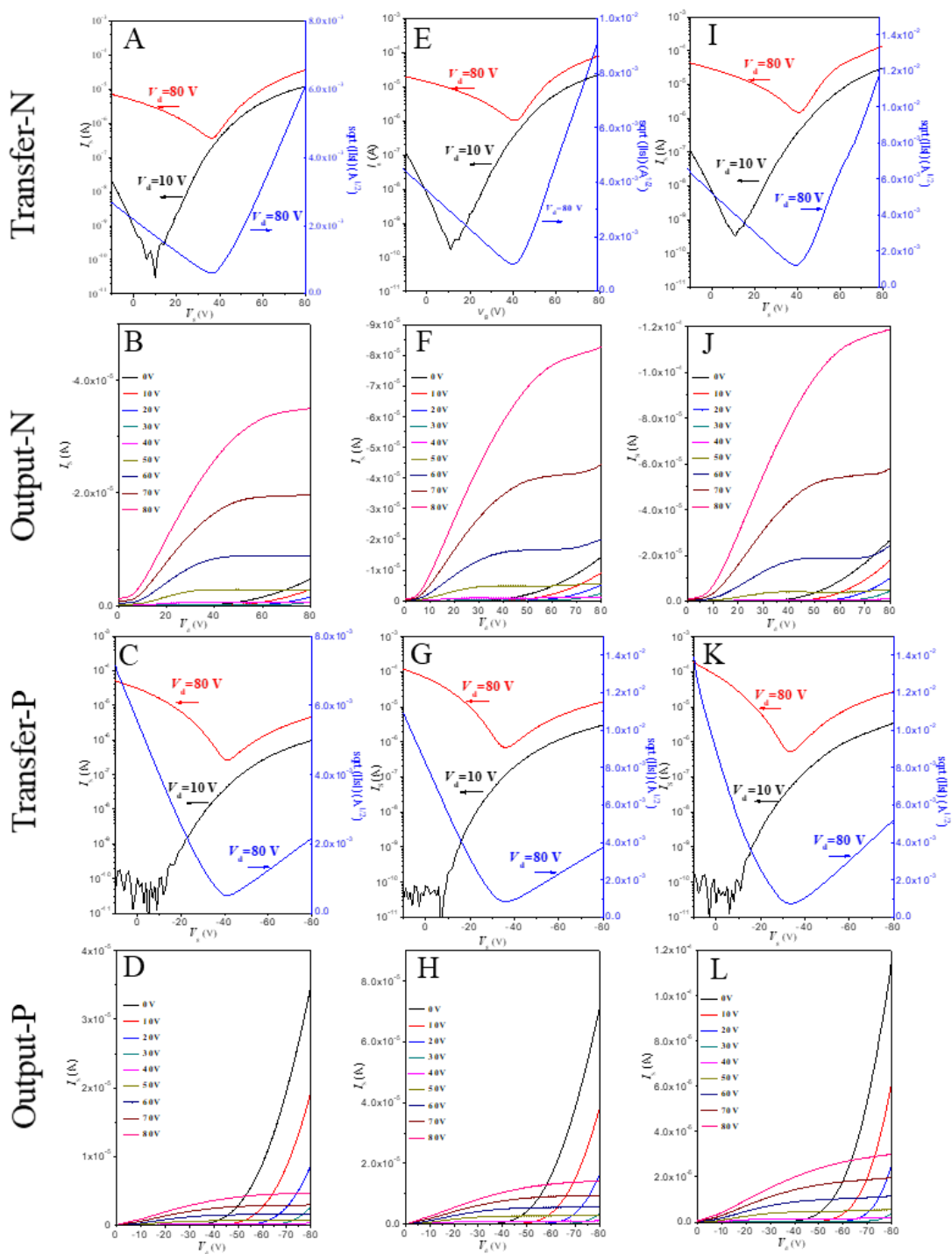


Figure S16. OTFT output and transfer characteristics of (A-D) ITIC-2Cl- δ ; (E-H) ITIC-2Cl- m ; (I-L) ITIC-2Cl- γ . Related to **Figure 5**.

Supplemental Tables

Table S1. The carrier lifetime (τ) and the determined sweeping out times (t_s) of **ITIC-2Cl- δ** , **ITIC-2Cl- m** and **ITIC-2Cl- γ** -based OSCs devices. Related to **Figure 6**.

Acceptors	τ (μ s)	t_s (μ s)	τ / t_s
ITIC-2Cl-δ	0.83	0.31	2.67
ITIC-2Cl-m	0.74	0.35	2.11
ITIC-2Cl-γ	1.12	0.29	3.86

Table S2. Photovoltaic Parameters of the Optimized OSCs of **ITIC-2Cl- δ** , **ITIC-2Cl- m** and **ITIC-2Cl- γ** -based devices with **PBDB-T2Cl**. Related to **Figure 5**.

Acceptors	V_{oc} (V)	J_{sc} (mA cm ⁻²)	FF (%)	PCE _{max} (%)
ITIC-2Cl-γ	0.92	18.79	65.10	11.25
ITIC-2Cl-δ	0.90	17.93	62.29	10.02
ITIC-2Cl-m	0.90	17.44	59.85	9.41

Table S3. OTFT performance parameters of **ITIC-2Cl- δ** , **ITIC-2Cl- m** and **ITIC-2Cl- γ** annealed under optimal conditions. Related to **Figure 5**.

Acceptors	T_a (°C)	n-channel				p-channel			
		$\mu_{e,lin}$	$\mu_{e,sat}$	V_t	On/Off	$\mu_{e,lin}$	$\mu_{e,sat}$	V_t	On/Off
		($\text{cm}^2 \text{V}^{-1} \text{s}^{-1}$)	($\text{cm}^2 \text{V}^{-1} \text{s}^{-1}$)	(V)		($\text{cm}^2 \text{V}^{-1} \text{s}^{-1}$)	($\text{cm}^2 \text{V}^{-1} \text{s}^{-1}$)	(V)	
ITIC-2Cl-δ	150	0.011	0.041	40	10^2	0.0027	0.0038	-30	10^2
ITIC-2Cl-m	150	0.0098	0.049	41	10^2	0.0049	0.0055	-29	10^2
ITIC-2Cl-γ	150	0.018	0.091	45	10^2	0.0066	0.010	-28	10^2

Supplemental References

1. Mihailechi, V. D., Wildeman, J., Blom, P. W. (2005). Space-Charge Limited Photocurrent. *Phys. Rev. Lett.* 94, 126602-126605.
2. Davids, P. S., Campbell, I. H., Smith, D. L. (1997). Device Model for Single Carrier Organic Diodes. *J. Appl. Phys.* 82, 6319-6325.
3. Lin, Y., Wang, J., Zhang, Z. G., Bai, H., Li, Y., Zhu, D., Zhan, X. (2015). An Electron Acceptor Challenging Fullerenes for Efficient Polymer Solar Cells. *Adv. Mater.* 27, 1170-1174.
4. Yao, H., Cui, Y., Yu, R., Gao, B., Zhang, H., Hou, J. (2017). Design, Synthesis, and Photovoltaic Characterization of a Small Molecular Acceptor with an Ultra-Narrow Band Gap. *Angew. Chem. Int. Ed.* 56, 3045-3049.
5. Li, Y., Lin, J.-D., Che, X., Qu, Y., Liu, F., Liao, L. S., Forrest, S. R. (2017). High Efficiency Near-Infrared and Semitransparent Non-Fullerene Acceptor Organic Photovoltaic Cells. *J. Am. Chem. Soc.* 139, 17114-17119.